










ATOMS: ALMA Three-millimeter Observations of Massive Star-forming regions – I. Survey description and a first look at G9.62+0.19

Tie Liu ,^{1,2,25}★ Neal J. Evans,^{2,3} Kee-Tae Kim ,^{2,4} Paul F. Goldsmith,⁵ Sheng-Yuan Liu,⁶ Qizhou Zhang,⁷ Ken’ichi Tatematsu ,⁸ Ke Wang,⁹ Mika Juvela ,¹⁰ Leonardo Bronfman,¹¹ Maria. R. Cunningham,¹² Guido Garay,¹¹ Tomoya Hirota ,⁸ Jeong-Eun Lee,¹³ Sung-Ju Kang,² Di Li ,^{14,15,16} Pak-Shing Li,¹⁷ Diego Mardones,¹¹ Sheng-Li Qin,¹⁸ Isabelle Ristorcelli,¹⁹ Anandmayee Tej,²⁰ L. Viktor Toth ,²¹ Jing-Wen Wu,¹⁴ Yue-Fang Wu,²² Hee-weon Yi,¹³ Hyeong-Sik Yun,¹³ Hong-Li Liu ,²³ Ya-Ping Peng,²⁴ Juan Li ,^{1,26} Shang-Huo Li,¹ Chang Won Lee,^{2,4} Zhi-Qiang Shen,^{1,26} Tapas Baug,⁹ Jun-Zhi Wang,^{1,26} Yong Zhang,²⁷ Namitha Issac,²⁰ Feng-Yao Zhu,¹ Qiu-Yi Luo,¹ Archana Soam ,²⁸ Xun-Chuan Liu,²² Feng-Wei Xu,²² Yu Wang,²² Chao Zhang,¹⁸ Zhiyuan Ren¹⁴ and Chao Zhang¹⁴

Affiliations are listed at the end of the paper

Accepted 2020 June 1. Received 2020 May 26; in original form 2020 April 13

ABSTRACT

The ATOMS, standing for ALMA Three-millimeter Observations of Massive Star-forming regions, survey has observed 146 active star-forming regions with ALMA band 3, aiming to systematically investigate the spatial distribution of various dense gas tracers in a large sample of Galactic massive clumps, to study the roles of stellar feedback in star formation, and to characterize filamentary structures inside massive clumps. In this work, the observations, data analysis, and example science of the ATOMS survey are presented, using a case study for the G9.62+0.19 complex. Toward this source, some transitions, commonly assumed to trace dense gas, including CS $J = 2-1$, HCO⁺ $J = 1-0$, and HCN $J = 1-0$, are found to show extended gas emission in low-density regions within the clump; less than 25 per cent of their emission is from dense cores. SO, CH₃OH, H¹³CN, and HC₃N show similar morphologies in their spatial distributions and reveal well the dense cores. Widespread narrow SiO emission is present (over ~ 1 pc), which may be caused by slow shocks from large-scale colliding flows or H II regions. Stellar feedback from an expanding H II region has greatly reshaped the natal clump, significantly changed the spatial distribution of gas, and may also account for the sequential high-mass star formation in the G9.62+0.19 complex. The ATOMS survey data can be jointly analysed with other survey data, e.g. MALT90, Orion B, EMPIRE, ALMA_IMF, and ALMAGAL, to deepen our understandings of ‘dense gas’ star formation scaling relations and massive protocluster formation.

Key words: stars: formation – stars: kinematics and dynamics; ISM: H II regions; ISM: clouds.

1 INTRODUCTION

Knowledge of the physical factors that control the conversion of interstellar gas into stars is of fundamental importance for understanding the star formation process and the evolution of

galaxies. Schmidt (1959) proposed a relation between star formation rate (SFR) and gas density. Kennicutt (1998a,b) found a strong observational relation between the SFR surface density (Σ_{SFR}) and the surface density of cold gas (Σ_{gas}), which suggests that the SFR surface density is primarily regulated by the gas mass surface density. This so-called Kennicutt–Schmidt (K–S) law, is a crucial input into theoretical models of galaxy evolution (e.g. Vogelsberger et al. 2014; Pillepich et al. 2018). The K–S law

* E-mail: liutieku@gmail.com; liutie@shao.ac.cn

between Σ_{SFR} and total gas surface density ($\Sigma_{\text{gas}} = \Sigma_{\text{HI}} + \Sigma_{\text{H}_2}$) across entire galaxies and galactic nuclei, has a typical power-law index of ~ 1.4 – 1.6 (Kennicutt 1998a,b; Kennicutt & Evans 2012). Resolved studies of nearby galaxies instead show a linear relation of Σ_{SFR} with molecular gas, implying a depletion time for gas that is constant with surface density at about 1–2 Gyr (e.g. Bigiel et al. 2008; Tacconi, Genzel & Sternberg 2020). While significant progress has been made in recent years, there are still fundamental aspects of the origin of star formation relations that remain unaddressed.

1.1 The role of dense molecular gas in star formation

Gao & Solomon (2004) showed that the far-infrared luminosities (L_{IR}) in starburst galaxies correlated tightly with the luminosities of HCN line emission, i.e. the dense gas star formation law. A nearly linear relation between SFR, indicated by L_{IR} , and dense molecular gas mass, indicated by molecular line luminosities (L'_{mol}), has been revealed in a number of entire galaxies (Gao & Solomon 2004; Greve 2014; Zhang et al. 2014; Liu et al. 2015a) or spatially resolved nearby galaxies (Chen et al. 2015; Tan et al. 2018) with various dense gas tracers, e.g. HCN, HCO^+ , CS, and high- J CO lines. The tightness of this correlation suggests that the denser parts of molecular clouds, rather than the total clouds, provide the direct fuel for star formation.

Wu et al. (2005, 2010) showed that massive, dense clumps (with typical sizes of ~ 1 pc) in the Milky Way followed a similar relation and suggested that the fundamental units of massive clustered star formation are such massive dense clumps. In addition, the vast majority of dense cores and young stellar objects (YSOs) in nearby clouds are found above a ‘threshold’ surface density of about $120 M_{\odot} \text{pc}^{-2}$ (or $A_V \sim 8$ mag) (Heiderman et al. 2010; Lada, Lombardi & Alves 2010; Lada et al. 2012). By comparing various models of star formation to observations of nearby clouds, Evans, Heiderman & Vutisalchavakul (2014) found that the mass of dense gas above such a ‘threshold’ surface density of $A_V \sim 8$ mag was the best predictor of the SFR. Vutisalchavakul, Evans & Heyer (2016) found a similar result for more distant and massive clouds in the Galactic plane, using millimeter continuum emission from the BGPS survey (Ginsburg et al. 2013) to measure the mass of dense gas. The average SFR per unit mass of dense gas (star formation efficiency; SFE) is remarkably constant from the scales of nearby molecular clouds to Galactic plane clouds to nearby galaxies to distant (ultra)luminous IR galaxies (Vutisalchavakul et al. 2016). In contrast, the SFR per unit mass of total molecular gas shows much more dispersion (Vutisalchavakul et al. 2016).

However, the dense gas star formation relation and the nature of the gas probed by dense gas tracers such as HCN, HCO^+ , and CS emission are still far from being well-understood. One attractive explanation for the low SFE in molecular clouds is that most clouds are not gravitationally bound, but only relatively dense regions (clumps) within them are bound (e.g. Dobbs, Burkert & Pringle 2011; Barnes, Hernandez & O’Dougherty 2016). This may also explain the tight relation between far-infrared luminosities and the luminosities of dense molecular tracers in molecular clumps, i.e. dense gas star formation law (e.g. Wu et al. 2005, 2010). Liu et al. (2016) studied the dense gas star formation law for 146 Galactic clumps, most of which are gravitationally bound. They found that the slopes of the $L_{\text{IR}}-L'_{\text{mol}}$ correlations vary for clumps with different dust temperatures and luminosity-to-mass ratios. Such behaviour seems to be a result of different evolutionary stages of the Galactic clumps (Liu et al. 2016; Stephens, Jackson & Whitaker 2016).

Recent observations of nearby clouds have also shown that some traditional high-density tracers, such as HCN (1–0) and HCO^+ (1–0), are also easily detected in extended translucent regions at typical densities of 500cm^{-3} and are poor tracers of dense structures such as filaments or cores (Kauffmann et al. 2017; Pety et al. 2017; Shimajiri et al. 2017). Most recently, Evans, Kim & Wu (2020) mapped six distant ($d \sim 3.5$ – 10.4 kpc) clouds in HCN (1–0) and HCO^+ (1–0) line emission with high sensitivity (rms ~ 0.1 K per 0.2km s^{-1} channel). They found that in all cases a substantial fraction (in most cases, the majority) of the total line luminosity arises in gas below the $A_V \sim 8$ mag threshold. These studies have challenged the definition of dense gas associated with the observation of some commonly used tracers, e.g. $J = 1$ – 0 of HCN and HCO^+ , but are limited in scope.

Therefore, in order to understand the origin of the dense gas star formation law, we need to address the following questions: (1) What is the spatial distribution of various molecular transitions, such as CS, HCN, and HCO^+ , in molecular clouds? (2) How much dense gas in the gravitationally bound clumps is actually participating in star formation or is concentrated in the smallest star formation units, i.e. dense cores that have typical sizes of ~ 0.1 pc? The project introduced in this paper will systematically study how these ‘dense gas’ tracers behave on small scales of clumps to cores, aiming for a thorough understanding of the dense gas star formation law.

For the remainder of this paper, we refer to CS, HCN, and HCO^+ without specifying the transitions. However, we emphasize that the sensitivity to density varies strongly with energy level; the transitions from levels higher than those in this study, e.g. $J = 2$ for CS, $J = 1$ for HCN and HCO^+ , are increasingly sensitive to higher densities. Multiple transitions of a single molecular species or possibly single transitions of different species can be indicative of the characteristic densities of a region.

1.2 The role of stellar feedback in star formation

Stellar feedback from massive stars can strongly influence their surrounding interstellar medium and regulate star formation through protostellar outflows, thermal feedback, photoionizing radiation, radiation pressure, main-sequence winds from hot stars or supernova explosions (e.g. Krumholz et al. 2014). The combined effects of multiple feedback mechanisms can significantly reduce SFRs and may play a major role in determining the SFE and the stellar initial mass function in molecular clouds (e.g. Krumholz et al. 2014). Although stellar feedback usually has a negative effect on star formation, in the sense of restraining or terminating star formation, it is also possible for feedback to be positive by triggering new star formation (e.g. Elmegreen & Lada 1977; Whitworth et al. 1994a,b; Krumholz et al. 2014; Wall et al. 2020). By studying a large sample of infrared bubbles, Thompson et al. (2012) estimated that the fraction of massive stars in the Milky Way formed by a triggering process could be between 14 and 30 per cent.

With ALMA, Liu et al. (2017) recently studied sequential high-mass star formation in a protocluster, the G9.62+0.19 complex. The ALMA observations resolved G9.62+0.19 into a massive filament that fragments into dozens of continuum sources that are at different evolutionary stages [from high-mass starless core candidates, high-mass protostellar objects (HMPOs), hot molecular cores, to ultracompact (UC) H II regions], as also suggested in other works (Garay et al. 1993; Hofner et al. 1994, 1996; Testi et al. 2000; Hofner, Wiesemeyer & Henning 2001; Liu et al. 2011; Dall’Olio et al. 2019). Liu et al. (2017) also found no evidence for widespread

low-mass protostellar core population in the G9.62+0.19 complex. They suggested that the sequential high-mass star formation in this region is the outcome of the stellar feedback from evolved H II regions formed in the same natal clump. The core fragmentation may be suppressed due to feedback from young OB protostars by heating the cores up and injecting turbulence through outflows, leading to an increase of their Jeans masses.

In addition, thermal feedback (from outflow heating, accretion luminosity, or radiative heating from OB protostars) enhanced by stellar radiation heating in conjunction with magnetic field can be important for reducing the level of fragmentation and producing massive stars (e.g. Offner, Klein & McKee 2009; Krumholz, Klein & McKee 2011; Myers et al. 2013). In contrast to the magnetic field, which is most effective in more diffuse regions, radiation feedback is more efficient in suppressing fragmentation in the dense, central region of protoclusters (Myers et al. 2013). Moscadelli et al. (2018) studied the feedback of a Hyper Compact (HC) H II region on its parental molecular core in the star-forming region G24.78+0.08. They found that the ionized gas of the HC H II region is expanding into the surrounding molecular gas. The shocks produced by the fast expansion of the ionized gas significantly influence the temperature distribution throughout its parental molecular core. In addition, outflows can also heat gas at parsec scale within clumps (e.g. Wang, Zhang & Wu 2012).

Studies of stellar feedback in protoclusters are still rare in cases. More systematic study is needed, however, to evaluate how formed OB protostars in protoclusters influence the dense gas distribution and SFE in their natal clumps. With its unprecedented sensitivity, ALMA enables such a systemic study, through observing a large sample of protoclusters in a very reasonable integration time.

1.3 The role of filaments in star formation

Thermal dust emission imaging surveys with the *Herschel Space Observatory* have discovered ubiquitous filamentary structures in nearby clouds and distant Galactic plane giant molecular clouds (GMCs) (e.g. André et al. 2010, 2014, 2019; Molinari et al. 2010; Arzoumanian et al. 2011; Juvela et al. 2012; Könyves et al. 2015; Wang et al. 2016; Arzoumanian et al. 2019; Schisano 2020). High-resolution images from the space telescope *Herschel* and ground-based telescopes reveal complex internal structures inside filamentary clouds, including dense cores along or at the intersections of some of the filamentary substructures (Wang, Zhang & Wu 2011; André et al. 2014; Wang et al. 2014; Könyves et al. 2015; Zhang, Wang & Lu 2015; Kainulainen et al. 2017; Liu et al. 2018a,b). Velocity coherent fiber-like substructures in filaments are also identified in nearby clouds (Hacar et al. 2013, 2016, 2018; González Lobos & Stutz 2019) and distant infrared dark clouds (IRDC; Chen et al. 2019). Observations by *Herschel* revealed that more than 70 per cent of pre-stellar cores are embedded in larger, parsec-scale filamentary structures in nearby molecular clouds (André et al. 2014; Könyves et al. 2015). The fact that the cores reside mostly within the densest filaments with column densities exceeding $\sim 7 \times 10^{21} \text{ cm}^{-2}$ strongly suggests a column density threshold for core formation (e.g. Enoch et al. 2007; André et al. 2014, and references therein).

In addition, filaments also play an important role in cluster formation (e.g. Stutz & Gould 2016; Stutz 2018). Hub-filament systems have been revealed in high-mass star-forming regions, implying a global hierarchical collapse scenario for protocluster formation (Liu et al. 2012, 2015b; Chen et al. 2019). Gas accreted along filaments continuously feeds the hub region, where massive

stars may form (Liu et al. 2012; Kirk et al. 2013; Peretto et al. 2013; Lu et al. 2018; Chen et al. 2019). To date, however, only a few observational studies have been performed to trace the hypothesized accretion flows along filaments in protoclusters.

Despite the importance of filaments in star formation, we still have too many missing links from observations to reconstruct a complete picture of star formation inside filaments. For example, do filaments in widely different environments, e.g. Galactic plane GMCs or nearby clouds, show similar properties? Are hub-filament systems common in high-mass star-forming regions? To deepen our understandings of the roles of filaments in star formation, we need to systematically investigate a sample of filaments in both far and near clouds across the Galaxy. To separate cores from filaments in distant massive clumps, we need resolution of $< 0.1 \text{ pc}$, which requires angular resolution of $< 2 \text{ arcsec}$ at distances of $< 10 \text{ kpc}$. Only with ALMA, such a systemic high-resolution observational study is possible.

2 ATOMS: ALMA THREE-MILLIMETER OBSERVATIONS OF 146 MASSIVE STAR-FORMING REGIONS

To statistically investigate the star formation process in the Galaxy, we initiated the ‘ALMA Three-millimeter Observations of Massive Star-forming regions (ATOMS)’ survey programme at ALMA. The main science goals of the ATOMS project are as follows:

- (i) to deepen the understandings of the dense gas star formation law by studying the spatial distributions of various dense gas tracers in a large sample of Galactic clumps and evaluating how much of molecular gas is participating in star formation;
- (ii) to investigate how stellar feedback from formed OB (proto)stars influences the surrounding gas distributions and the next generation of star formation in their natal clumps;
- (iii) to resolve filaments and to study their roles in protocluster formation.

2.1 The sample of ATOMS

The ATOMS sample of 146 sources was selected from the CS $J = 2-1$ survey of Bronfman, Nyman & May (1996), a complete and homogenous molecular line survey of UC H II region candidates in the Galactic plane. The sample of our 146 targets is complete for protoclusters with bright CS $J = 2-1$ emission ($T_b > 2 \text{ K}$), indicative of reasonably dense gas. It is also complete for the longitude range observable by SEST as well as ALMA (Faúndez et al. 2004). Table A1 lists the basic parameters of this sample, including source IDs in observations (column 1), IRAS names (column 2), coordinates (columns 3–4), systemic velocities (V_{lsr} , column 5), distances from the sun (column 6), Galactocentric distances (R_{GC} , column 7), effective radii (R_{eff} , column 8), dust temperature (T_{dust} , column 9), bolometric luminosity (L_{bol} , column 10), and clump masses (M_{clump} , column 11). There are 122 clumps with ATLASGAL and HiGAL counterparts, which have been analysed in detail by Urquhart, König & Giannetti (2018). The basic parameters for these 122 clumps are adopted from Urquhart et al. (2018). The basic parameters for the remaining clumps are adopted from Faúndez et al. (2004).

Fig. 1 shows the Galactic distribution of the ATOMS targets on the *Planck* 857 GHz emission map. Fig. 2 presents the spatial distribution of the ATOMS targets on a top-down schematic view of the Milky Way. From them, we can see that most (139) of

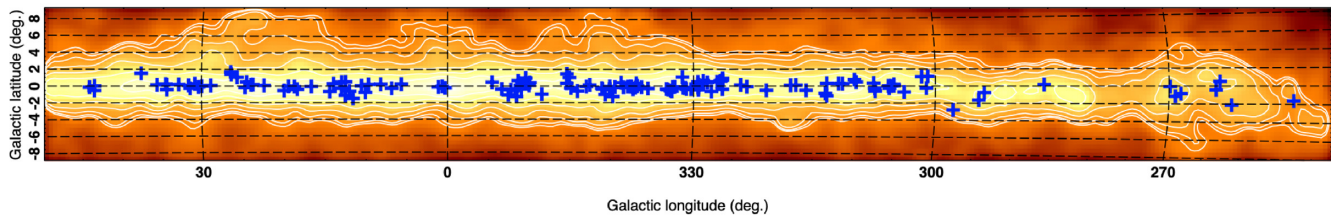


Figure 1. Galactic distribution of the ATOMS targets ('+'). The background image and contours show *Planck* 857 GHz emission. The contours are from 34.6 to 874.5 MJy sr⁻¹ with 10 steps on a logarithmic scale.

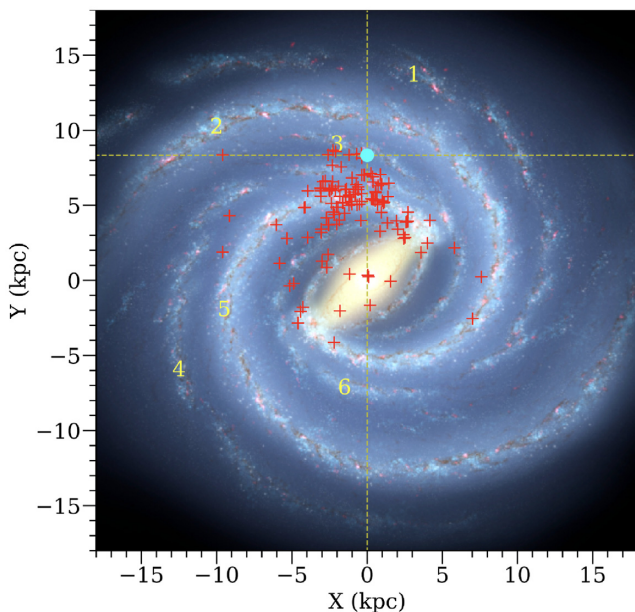


Figure 2. Spatial distribution of the ATOMS targets ('+') projected on to a top-down schematic view of the Milky Way (artist's concept, R. Hurt: NASA/JPLCaltech/SSC). The spiral arms are indicated using numbers from 1 to 6, referring to the Outer, Perseus, Local, Carina-Sagittarius, Scutum-Centaurus, and Norma arms. [Codes used for this plot are from Yuan et al. (2017)].

the ATOMS targets are located in the first and fourth Galactic Quadrants of the inner Galactic plane ($|b| < 2^\circ$). The distances of the sample clouds range from 0.4 to 13.0 kpc with a mean value of 4.5 kpc. About 67 percent of the sources are located closer than ~ 5 kpc (see Fig. 2). We include 27 distant ($d > 7$ kpc) sources that are either close to the Galactic Centre or mini-starbursts (like W49N/I19078+0901), representing extreme environments for star formation. The sources have Galactocentric distances ranging from 0.5 to 12.7 kpc, and are mostly located on spiral arms (see Fig. 2).

Fig. 3(a) presents the distribution of the clump masses of the sample. The clump masses range from 5.6 to $2.5 \times 10^5 M_\odot$, with a median value of $1.4 \times 10^3 M_\odot$. The distribution of the bolometric luminosity of targets is shown in Fig. 3(b). The bolometric luminosity ranges from 16 to $8.1 \times 10^6 L_\odot$, with a median value of $5.7 \times 10^4 L_\odot$. All the targets in the sample have bolometric luminosity larger than $1 \times 10^3 L_\odot$ except for I08076–3556 and I11590–6452. I08076–3556, also known as BHR 12 or CG 30, is a bright-rimmed cometary globule located in the Gum Nebula region at a distance of ~ 400 pc, in which a low-mass binary system is forming (Chen et al. 2008). I11590–6452 (also known as BHR 71)

is also a bright-rimmed cometary globule that is forming a wide binary system (Tobin, Bourke & Mader 2019).

The radii of the sample range from 0.06 to 4.26 pc, with a median value of 0.86 pc, suggesting that the sample contains both nearby dense cores ($R_{\text{eff}} \sim 0.1$ pc) and distant clouds (R_{eff} of several pc). The dust temperature ranges from 18 to 46 K, with a median value of 29 K. Liu et al. (2016) observed this sample in HCN (4–3) and CS (7–6) lines. The linewidths of HCN (4–3) range from 1.5 to 21 km s⁻¹, with a median value of 6.4 km s⁻¹. The linewidths of CS (7–6) range from 1.6 to 23 km s⁻¹, with a median value of 4.5 km s⁻¹. Most of the targets tend to be gravitationally bound with an average virial parameter of ~ 0.8 (Liu et al. 2016).

In a word, this is a very diverse sample that is suitable for statistical studies of the star formation process with different conditions, e.g. different density, temperature, turbulence level, and luminosity of dominating OB protostars, in widely different Galactic environments covering a large range of Galactocentric distances.

Fig. 3(c) shows the mass–radius diagram for the ATOMS sample. All the targets are above the mass surface density thresholds for ‘efficient star formation’ given in Lada et al. (2010) and Heiderman et al. (2010), implying that they are active star-forming regions. We notice that only three of the ATOMS targets are above the surface density threshold of 1 g cm^{-2} , which is a stringent threshold for high-mass star formation given by Krumholz & McKee (2008). However, there are 134 clumps having mass surface density above the threshold for high-mass star formation regions, $M > 870 M_\odot (r/\text{pc})^{1.33}$, defined by Kauffmann & Pillai (2010). Based on studies of ATLASGAL clumps, Urquhart et al. (2014) also suggested a less stringent empirical threshold of 0.05 g cm^{-2} for high-mass star formation. There are 132 clumps fulfilling the thresholds given by Kauffmann & Pillai (2010) and Urquhart et al. (2014), suggesting that more than 90 percent of the ATOMS targets have the ability to form high-mass stars. Fig. 3(d) shows the luminosity–mass diagram for the ATOMS sample. About 143 ATOMS targets are above the evolution tracks for stars with final masses larger than $8 M_\odot$, indicating that the majority of the clouds are forming high-mass stars. The majority of the clumps are in the accelerated accretion phase (Molinari et al. 2008).

In the following sections, we describe the observations, data analysis, and illustrate the science goals of the ATOMS survey, using a case study for the G9.62+0.19 clump (known as I18032–2032 in Table A1), which is an active high-mass star-forming region located at a distance of $5.2_{-0.6}^{+0.6}$ kpc (from trigonometric parallax of 12 GHz methanol masers; Sanna et al. 2009). The G9.62+0.19 clump is unstable against gravitational collapse even if thermal, turbulent, and magnetic field support are taken into account together (Liu et al. 2018c). We should note that throughout this paper the analysis of G9.62+0.19 and comparison with previous works, e.g. Liu et al. (2017), is only applicable to this particular source. The

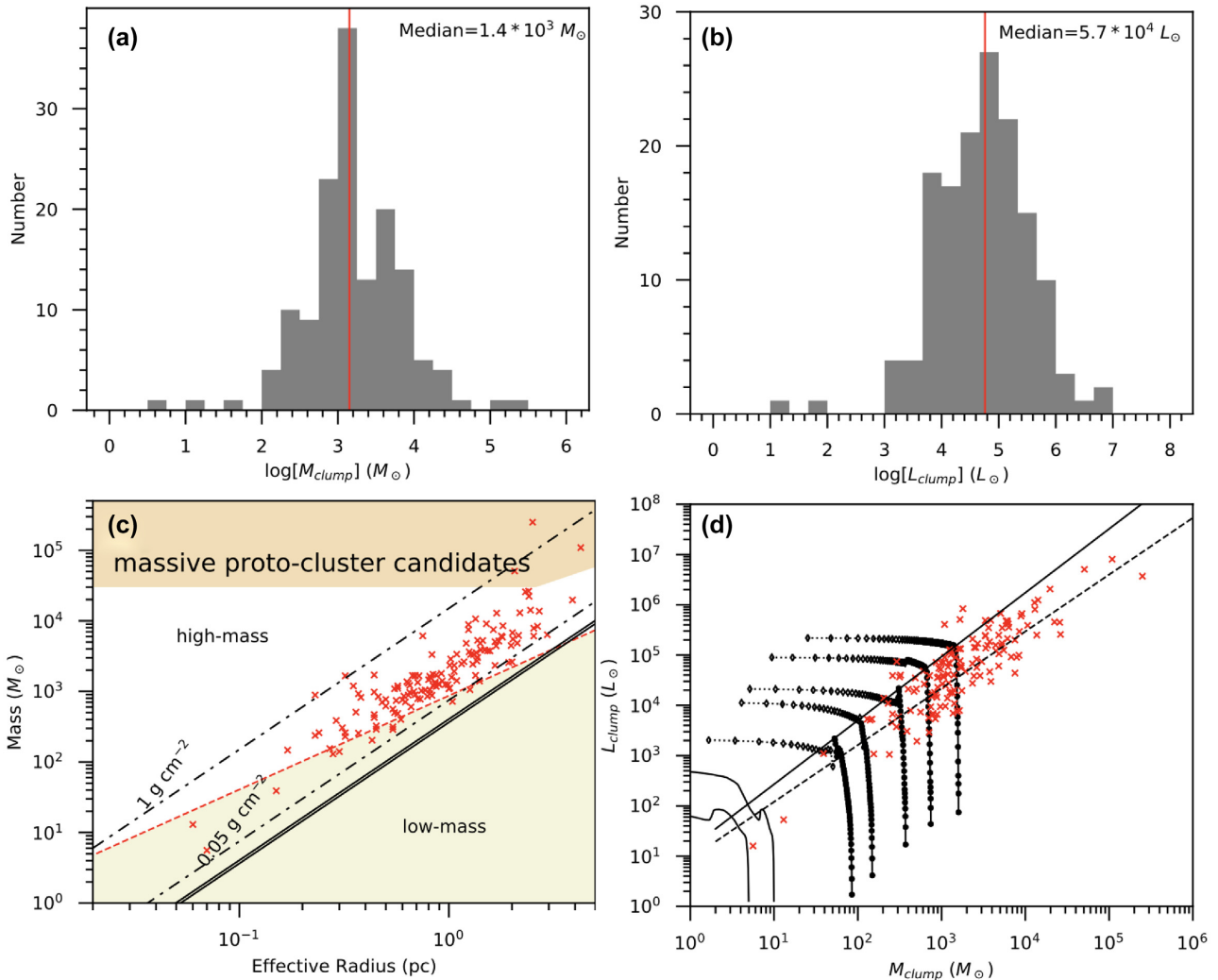


Figure 3. (a) Distribution of clump masses of the ATOMS targets; the red line shows the median value; (b) Distribution of clump luminosity; (c) M_{clump} as a function of effective radii for ATOMS targets (red crosses). The unshaded area (above the red dashed line) delimits the region of high-mass star formation regions above the threshold $M > 870 M_{\odot} (r/\text{pc})^{1.33}$ defined by Kauffmann & Pillai (2010). The black solid lines show the mass surface density thresholds for ‘efficient star formation’ of $116 M_{\odot} \text{pc}^{-2}$ ($\sim 0.024 \text{g cm}^{-2}$) from Lada et al. (2010) and $129 M_{\odot} \text{pc}^{-2}$ ($\sim 0.027 \text{g cm}^{-2}$) from Heiderman et al. (2010). The upper and lower dot-dashed lines show two mass surface density thresholds of 0.05 and 1g cm^{-2} for high-mass star formation, which are given by Urquhart et al. (2014) and Krumholz & McKee (2008), respectively. The upper shaded region indicates the parameter space for massive protoclusters, defined in Bressert et al. (2012). (d) Luminosity–mass diagram for ATOMS targets (red ‘+’). Evolutionary tracks for stars with final masses of 2.0, 4.0, 6.5, 8.0, 13.5, 18.0, and $35.0 M_{\odot}$ are from Saraceno et al. (1996, solid tracks) and Molinari et al. (2008, tracks with symbols). The solid and dashed lines are the best log–log fit for Class I and Class 0 sources, respectively, extrapolated in the high-mass regime by Molinari et al. (2008). Codes used for panels (c) and (d) are from Yuan et al. (2017).

ATOMS will allow to extend the analysis to a much larger sample of sources.

2.2 ALMA observations

The ALMA observations of the ATOMS survey were conducted from late September to mid November 2019 with both the Atacama Compact 7-m Array (ACA; Morita Array) and the 12-m array (C43-2 or C43-3 configurations) with band 3 (Project ID: 2019.1.00685.S; PI: Tie Liu). The observations including source IDs, observation dates, minimum baselines, maximum baselines, angular resolution, maximum recovering scale (MRS), and rms level per 0.122 MHz channel in the ATOMS survey are summarized in Table 1. The ACA observations of G9.62+0.19 (I18032–2032, number 108 in Table 1)

were conducted on 2019 October 1 and 13, with two executions. The 12-m-array observations of G9.62+0.19 were conducted on 2019 October 31.

We conducted single-pointing observations with ALMA. The typical 12-m-array time on source is ~ 3 min, while typical ACA observing time per source is ~ 8 min. The angular resolution and maximum recovered angular scale for the ACA observations are ~ 13.1 – 13.8 and 53.8 – 76.2 arcsec, respectively. The angular resolution and maximum recovering angular scale for the 12-m-array observations are ~ 1.2 – 1.9 and 14.5 – 20.3 arcsec, respectively. These ACA and 12-m-array observations are sensitive to angular scales smaller than ~ 60 and 20 arcsec, respectively. The achieved angular resolutions of the 12-m-array observations are usually better than 2 arcsec, enabling us to resolve dense cores (~ 0.1 pc in size;

Table 1. Observation logs of the ATOMS survey.

Source IDs	Observation date	Min BL (m)	Max BL (m)	Angular resolution (arcsec)	Maximum recovering scale (arcsec)	rms per 0.122 MHz channel (mJy beam ⁻¹)
ACA observations						
1	2019-10-14	8.9	48.0	13.3	76.2	49
2–7	2019-10-14	8.9	48.0	13.3	76.2	63
8	2019-10-19	8.9	48.0	13.3	72.9	46
9–11	2019-11-08	8.9	48.0	13.3	76.2	70
12–23	2019-11-15	8.9	48.0	13.3	76.2	70
24–30	2019-11-13, 2019-11-17	8.9	44.7	13.5	76.2	70
31–36	2019-11-12	9.6	48.0	13.1	53.8	61
37–62	2019-11-17, 2019-11-18	8.9	48.0	13.3	76.2	61
63–81	2019-11-12	8.9	48.0	13.1	76.2	93
82–88	2019-10-31	8.9	45.0	13.8	76.2	58
89–101	2019-11-19	8.9	48.0	13.3	76.2	83
102–104	2019-09-30	9.6	48.0	13.1	53.8	51
105–110	2019-10-01, 2019-10-13	9.1	48.0	13.1	65.4	48
111–123	2019-11-02, 2019-11-03	8.9	44.7	13.5	76.2	80
124–131	2019-10-31, 2019-11-01	8.9	48.0	13.3	76.2	51
132–143	2019-11-01, 2019-11-04	8.9	48.0	13.3	76.2	64
144–146	2019-09-30	9.6	48.0	13.1	53.8	67
ALMA 12-m observations						
1	2019-10-19	15.1	783.5	1.2	14.5	3.7
2–7	2019-10-19	15.1	783.5	1.2	14.5	4.5
8	2019-11-02	15.1	500.2	1.7	19.0	6.2
9–11	2019-11-11	15.1	500.2	1.8	20.3	8.1
12–23	2019-11-13	15.3	500.2	1.7	19.3	9.3
24–30	2019-11-12	15.1	500.2	1.8	19.5	9.6
31–36	2019-11-04	15.1	500.2	1.8	20.3	5.9
37–62	2019-11-04	15.1	500.2	1.7	19.9	9.0
63–81	2019-11-03	15.1	500.2	1.7	20.1	6.4
82–88	2019-11-03	15.1	500.2	1.9	21.1	9.2
89–101	2019-11-03	15.1	500.2	1.7	20.1	8.4
102–104	2019-10-28	15.1	696.8	1.4	18.1	6.6
105–110	2019-10-31	15.1	696.8	1.5	19.9	8.1
111–123	2019-11-01	15.1	500.2	1.7	18.3	8.5
124–131	2019-10-31	15.1	696.8	1.5	19.9	7.4
132–143	2019-10-31	15.1	696.8	1.5	19.9	5.4
144–146	2019-10-31	15.1	696.8	1.5	19.9	7.9

or 2 arcsec at 10 kpc distance) in the most distant sources. The obtained sensitivity in 12-m-array observations ranges from 3.7 to 9.6 mJy beam per 0.122 MHz channel.

The observations employed the band 3 receivers in dual-polarization mode. Eight spectral windows (SPWs) were configured to cover 11 commonly used lines including the dense gas tracers (e.g. $J = 1-0$ of HCO^+ , HCN and their isotopes), hot core tracers (e.g. CH_3OH , HC_3N), shock tracers (e.g. SiO , SO), and ionized gas tracers ($\text{H}_{40\alpha}$), as listed in Table 2. The second and third columns of Table 2 list the total bandwidth and spectral resolution of each SPW (column 1). The specie names, transitions, rest frequencies, and upper energies are listed in columns 4–7. The critical density (n_{crit}), as the density for which the net radiative decay rate from j to k equals the rate of collisional depopulation out of the upper level j for a multilevel system, of these transitions at 100 K are shown in the eighth column. In the ninth column, we also listed the effective excitation density (n_{eff}) at 100 K, the density which results in a molecular line with an integrated intensity of 1 K km s^{-1} (Evans 1999; Shirley 2015).

Two wide SPWs, each one having 1875 MHz bandwidth and $\sim 3 \text{ km s}^{-1}$ spectral resolution, are used for continuum emission and line scan surveys. The SPWs (1–6) at the lower band have

sufficiently high spectral resolution ($\sim 0.2-0.4 \text{ km s}^{-1}$) to resolve line profiles in high-mass star-forming regions (typical linewidth of several km s^{-1}) for studying kinematics.

Calibration and imaging were carried out using the CASA software package version 5.6 (McMullin et al. 2007). The ACA data and 12-m-array data were calibrated and imaged separately.

The ACA data and 12-m-array data can be combined together to recover very extended emission that is missed in 12-m-array observations. In Fig. 4, we simply combine the 12-m-array data and ACA data of G9.62+0.19 in Fourier space with the CASA task ‘feather’ for HCO^+ and H^{13}CO^+ . Panels (a) and (c) of Fig. 4 present the spectra of HCO^+ and H^{13}CO^+ , respectively. We found that 12-m-array data alone has recovered more than 90 per cent of the flux in both H^{13}CO^+ and HCO^+ emission. Panels (b) and (d) of Fig. 4 show their integrated intensity maps from 1.5 to 6.5 km s^{-1} . The morphology of integrated intensity maps constructed with 12-m-array data alone is nearly identical to that of the maps constructed with combined data (see Figs 4b and d). We will more properly combine the ACA data and 12-m-array data in future studies and discuss the data combination issue in a forthcoming paper (Wang et al., in preparation). The combined data, however, also suffer a non trivial missing flux problem without zero-spacing information from

Table 2. Main targeted lines in the ATOMS survey.

SPW	Bandwidth (MHz)	δV (km s ⁻¹)	Species	Transition	Rest frequency (GHz)	E_u/k (K)	n_{crit}^a (100 K) (cm ⁻³)	n_{eff}^a (100 K) (cm ⁻³)	Note
SPW1	58.59	0.424	H ¹³ CN	1–0	86.339918	4.14	9.7×10^4	6.5×10^4	High-density tracer
SPW2	58.59	0.422	H ¹³ CO ⁺	1–0	86.754288	4.16	2.0×10^4	1.1×10^4	High-density and ionization tracer
SPW3	58.59	0.419	CCH	1–0	87.316898	4.19	1.9×10^5		Tracer of photodissociation regions
SPW4	58.59	0.421	SiO	2–1	86.84696	6.25	1.7×10^5		Shock/outflow tracer
SPW5	58.59	0.206	HCN	1–0	88.631847	4.25	1.1×10^5	1.7×10^3	High-density/infall/outflow tracer
SPW6	58.59	0.205	HCO ⁺	1–0	89.188526	4.28	2.3×10^4	2.6×10^2	High-density/infall/outflow tracer
SPW7	1875.00	2.973	CH ₃ OH	2(1,1)–1(1,0)A	97.582798	21.56	4.8×10^4		High-density/hot cores/shock tracer
			CS	2–1	97.980953	7.05	5.5×10^4	4.7×10^3	High-density/infall/outflow tracer
			SO	3(2)–2(1)	99.29987	9.23	3.0×10^5		High-density/shock/outflow tracer
			H ₂	H _{40α}	99.022952				Tracer of ionized gas/H II regions
SPW8	1875.00	2.914	HC ₃ N	11–10	100.07639	28.82	9.2×10^4	1.1×10^4	High-density/hot-cores tracer

^aThe critical density and effective excitation density are from Shirley (2015).

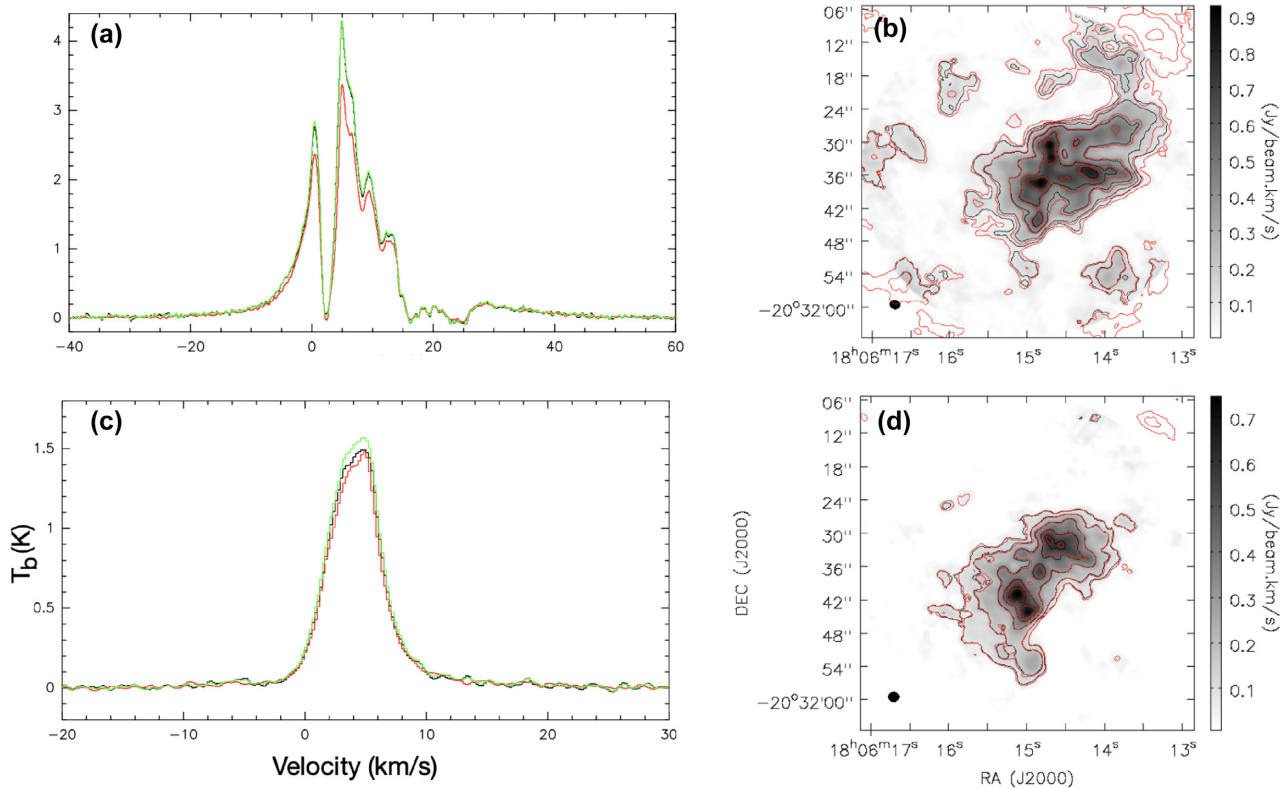


Figure 4. (a) HCO⁺ spectra in G9.62+0.19 averaged over a 30-arcsec region at the central position [R.A.(J2000) = 18:06:14.99, decl.(J2000) = –20:31:35.4]. The spectra from ACA data, 12-m-array data and combined 12-m and ACA data are shown in black, red, and green, respectively. (b) Comparison of the integrated intensity maps of HCO⁺ emission from 12-m-array data (grey image and black contours) and combined data (red contours). The contours are $[0.1, 0.2, 0.4, 0.6, 0.8] \times F_{\text{peak}}$. The peak integrated intensities (F_{peak}) in 12-m-array data and in combined data are 0.93 and 0.96 Jy beam⁻¹ km s⁻¹, respectively. (c) Same as in panel (a) but for H¹³CO⁺. (d) Same as in panel (b) but for H¹³CO⁺. The peak integrated intensities (F_{peak}) in 12-m-array data and in combined data are the same as 0.75 Jy beam⁻¹ km s⁻¹.

Total-Power (TP) observations. However, this is also advantageous for studying dense structures inside these ATOMS clumps. This filters out the large scale emission, making it easier the identification of compact cores or dense filamentary structures (see Sections 3.1 and 3.2.6). We should note that dense cores are usually very compact (see Table 3, for example) and have angular sizes much smaller than the maximum recovering angular scale (~ 20 arcsec) in the 12-m-array observations, indicating that the missing flux will not be a problem in deriving physical parameters (like fluxes,

densities, and masses) for dense cores using the 3-mm continuum emission.

In this work, we mainly focus on the spatial distributions of various gas tracers. The 12-m-array data alone are good enough for this purpose. Hence, in this paper, the ACA data and 12-m-array data were not combined for the case study of G9.62+0.19.

We construct continuum visibility data using the line-free spectral channels for G9.62+0.19. The continuum image of G9.62+0.19 from 12-m-array data reaches a 1σ rms noise of 0.2 mJy in a

Table 3. Parameters of continuum sources in G9.62+0.19.

Name	size	3-mm continuum			I_p^a (mJy beam ⁻¹)	$H_{40\alpha}$ V_{lsr} (km s ⁻¹)	FWHM (km s ⁻¹)
		I (mJy beam ⁻¹)	S_{ν} (mJy)	$S_{\text{free-free}}$ (mJy)			
B	15.30×13.31 arcsec ² (142°)	4.6	437	359	5.0	3.2	20.0
MM1/C	3.01×2.10 arcsec ² (132°)	8.17	32.6	32	6.6	0.2	20.4
MM4/E	1.28×1.02 arcsec ² (89°)	25.4	40.9	<2	<3		<20
MM6	1.75×1.05 arcsec ² (173°)	5.4	10.4				
MM7/G		5.7	5.7				
MM8/F	2.53×1.28 arcsec ² (166°)	13.2	35.5	<3	<3		<20
MM11/D	1.04×0.74 arcsec ² (72°)	71.6	98.8	73	17.8	11.8	25.8

^aThe values for MM4/E and MM8/F are upper limits based on rms level.

synthesized beam of 1.56×1.38 arcsec² (PA = 87°:62). The synthesized beams for molecular lines of G9.62+0.19 are slightly different from those for continuum. The typical synthesized beam is 1.9×1.7 arcsec² for lines at lower band (SPWs 1–6), and is 1.6×1.4 arcsec² for lines at upper band (SPWs 7–8). The 1σ rms noise is about 8 mJy beam⁻¹ at SPWs 1–4 per 0.122 MHz channel. SPWs 5–6 have the best spectral resolution of 0.06 MHz and their 1σ rms noise is about 10 mJy beam⁻¹ per channel. The 1σ rms noise at the two wide SPWs is about 3 mJy beam⁻¹ per channel. The continuum image constructed from ACA data reaches a 1σ rms noise of 4 mJy in a synthesized beam of 17.23×9.46 arcsec² (PA = -82°:87). The 1σ rms noise for the ACA observations are $\sim 40, 80,$ and 15 mJy beam⁻¹ per channel for lines in SPW 1–4, SPWs 5–6, and SPWs 7–8, respectively. The angular resolution and sensitivity achieved in observations of G9.62+0.19 are comparable to the median values of the whole sample.

3 SCIENCE GOALS AND A FIRST LOOK AT G9.62+0.19

In this section, we present the case study of the protocluster complex, G9.62+0.19, and introduce the exemplar sciences cases that can be addressed with the ATOMS survey.

3.1 Filaments and dense cores

The 3-mm continuum emission will be used to study how the massive clumps fragment into filaments and individual dense cores that will form new stars.

Fig. 5 shows the 3-mm continuum emission of G9.62+0.19. The 3-mm continuum emission from ACA observations is shown as contours in Fig. 5(a) and reveals only one single clump. The 3-mm continuum emission from high-resolution 12-m-array data is shown as grey image in Fig. 5(a) and contours in Fig. 5(b), which reveals the expanding cometary-like H II region, ‘B’, to the west, and a massive fragmented filament to the east.

In the ATOMS survey, we apply the FellWalker algorithm in the Starlink CUPID package (Berry et al. 2007, 2015), for source extraction. The core of the FellWalker algorithm is a gradient-tracing scheme consisting of following many different paths of steepest ascent in order to reach a significant summit, each of which is associated with a clump (Berry et al. 2007). FellWalker is less dependent on specific parameter settings than CLUMPFIND (Berry et al. 2007), and has been widely used in continuum surveys

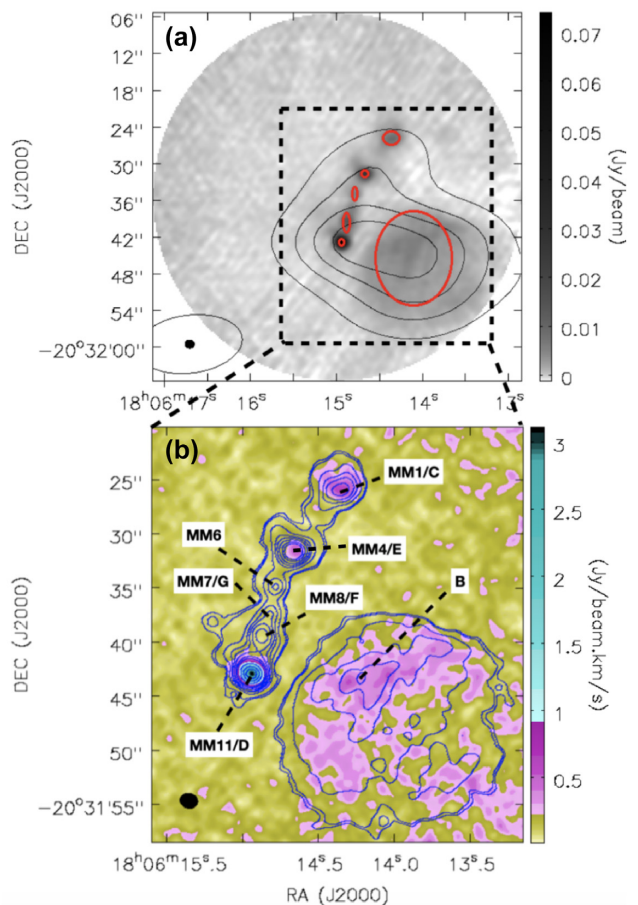


Figure 5. The 3-mm continuum emission of G9.62+0.19. (a) The 3-mm continuum emission from ACA observations is shown as contours at $[0.2, 0.4, 0.6, 0.8] \times 0.225$ Jy beam⁻¹. The starting (faintest) contour corresponds to $\sim 10\sigma$ ($\sigma = 4$ mJy beam⁻¹). The background image is the 3-mm continuum emission from the 12-m-array observations. The red ellipses show the continuum sources identified with FellWalker. (b) The 3-mm continuum emission from 12-m-array observations is shown as blue contours with contour levels of $[0.01, 0.013, 0.03, 0.05, 0.07, 0.1, 0.15, 0.2, 0.4, 0.6, 0.8] \times 74.1$ mJy beam⁻¹. The starting (faintest) contour corresponds to $\sim 3.5\sigma$ ($\sigma = 0.2$ mJy beam⁻¹). The background (coloured) image is the intensity of the $H_{40\alpha}$ line integrated from -50 to 50 km s⁻¹. The names (from Liu et al. 2017) of seven main components in the 3-mm continuum emission are indicated in the image.

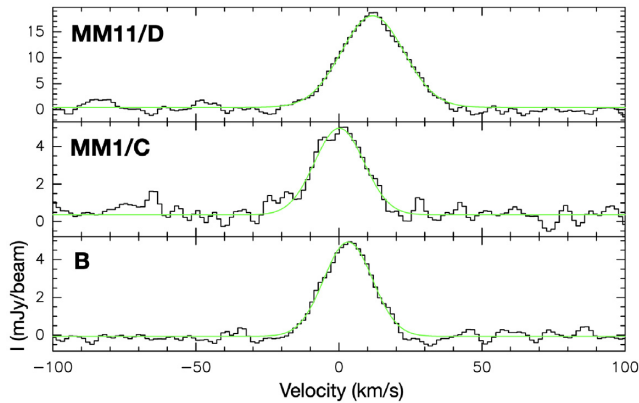


Figure 6. Source-averaged $H_{40\alpha}$ RRL in G9.62+0.19. The green lines are Gaussian fits.

(e.g. Eden et al. 2017, 2019; Liu et al. 2018a). Source extraction was conducted in regions above a threshold of 3σ . The minimum number of contiguous pixels (pixel size = 0.27 arcsec) was set at 12, equaling to those contained in half of the synthesized beam, which was used to define the smallest structures, i.e. ‘cores’ (see Sanhueza et al. 2019). We also tested FellWalker with a larger minimum number (16 and 25) of contiguous pixels and found that the results were not changed. The detected sources were fitted with a 2D Gaussian profile and de-convolved with the beam size. With FellWalker, we identified six main components in the 3-mm continuum emission of G9.62+0.19, as shown in Fig. 5(a). Their de-convolved sizes, peak flux density, and total flux density of the 3-mm continuum emission are listed in columns 2–4 of Table 3. Another component, MM7/G, is not resolved in 3-mm continuum, but is resolved in other hot core tracers like HC_3N (11–10). MM7/G is also marked on Fig. 5(b) and listed in Table 3.

At 3-mm, both thermal dust emission and free–free emission from ionized gas could contribute to the continuum emission. However, since not all the ATOMS targets have been observed at centimetre wavelengths, we cannot easily compile centimetre continuum emission data to help removing any free–free contribution to the 3-mm continuum emission. Instead, we use the $H_{40\alpha}$ radio recombination line (RRL) to estimate the contribution of free–free emission in continuum by deriving the line-to-continuum intensity ratio (Condon & Ransom 2016; Liu, Chen & Román-Zúñiga 2019). The integrated intensity map of $H_{40\alpha}$ is shown as colour image in Fig. 5(b). $H_{40\alpha}$ is clearly detected towards ‘B’, ‘MM1/C’, and ‘MM11/D’, and is marginally detected toward MM4/E. Fig. 6 presents the source-averaged $H_{40\alpha}$ spectra. The spectra were fitted with Gaussian profiles, and the fit results (peak intensity I_p , systemic velocity V_{lsr} , and linewidth FWHM) are summarized in columns 6–8 of Table 3. The linewidths of $H_{40\alpha}$ of ‘B’ and ‘MM1/C’ are $\sim 20 \text{ km s}^{-1}$. ‘MM11/D’ has the largest linewidth ($\sim 25 \text{ km s}^{-1}$) and velocity ($\sim 12 \text{ km s}^{-1}$) in $H_{40\alpha}$ line emission. The velocity ($\sim 12 \text{ km s}^{-1}$) of ionized gas in ‘MM11/D’ is significantly redshifted relative to that ($\sim 4.5 \text{ km s}^{-1}$) of the molecular gas, indicating a fast flow in the ionized gas as also seen in the HC HII region G24.78+0.08 (Moscadelli et al. 2018).

We estimated the free–free emission at 3-mm for ‘B’, ‘MM1/C’, and ‘MM11/D’, which are listed in column 5 of Table 3. An electron temperature of $\sim 6760 \text{ K}$ is adopted, which is derived from the electron temperature gradient in the Galactic disc (Quiroza et al. 2006). Higher electron temperature will lead to higher free–free emission contributions. The electron temperature could be better

constrained by observing multiple RRLs in future (Zhu et al. 2019). We found that the 3-mm continuum emission in ‘B’, ‘MM1/C’, and ‘MM11/D’ is dominated by free–free emission, as suggested in previous works (Hofner et al. 1996). The free–free emission in other sources is negligible. Since the properties of all the continuum sources have been well discussed in Liu et al. (2017), we will not derive any other parameters from the 3-mm continuum emission in this work.

Fragmented massive filaments are commonly seen in IRDCs (Wang et al. 2011, 2012, 2014, 2016; Zhang & Wang 2011; Zhang et al. 2015; Sanhueza et al. 2019). Those massive filaments in IRDCs also fragment into a chain of dense cores as seen in G9.62+0.19. However, those filaments in IRDCs seem to be undergoing cylindrical fragmentation governed by turbulence (Wang et al. 2011, 2014). In contrast, the fragmentation of the massive filament in G9.62+0.19 can be well explained by thermal Jeans instability (Liu et al. 2017).

Within the ATOMS project, we will systematically investigate the fragmentation process of protoclusters as G9.62+0.19, and compare with IRDC clumps. This will help figure out the dominating mechanisms in dense-core formation in different Galactic environments and conditions.

3.2 Spatial distribution of molecules

One of the main science goals of the ATOMS project is to investigate the small-scale distributions of various molecular gas tracers within massive star-forming regions. In particular, we will be more focused on those dense gas tracers, e.g. $J = 1-0$ of HCN and HCO^+ , and $J = 2-1$ of CS, which are commonly used in studying star formation scaling relations. By comparing with observational results in nearby clouds (Kauffmann et al. 2017; Pety et al. 2017; Shimajiri et al. 2017), we will investigate how well those gas tracers unveil the structures and masses of molecular clumps that are located in different Galactic environments and have different physical conditions, e.g. density, temperature, and UV radiation.

3.2.1 Gas clumps in ACA observations of G9.62+0.19

The ACA observations have large FOV (~ 2 arcmin) and maximum recovering scale (MRS; ~ 1 arcmin), enabling us to study the overall properties of gas emission at clump scale, such as total line luminosity, emission extent, and virial masses (Liu et al. 2020). Fig. 7 presents the integrated intensity (from 1.5 to 6.5 km s^{-1}) maps of various gas tracers in ACA observations of G9.62+0.19. All the gas tracers reveal a single gas clump that can be well modelled by a 2D Gaussian profile. We performed 2D Gaussian fitting in the gas emission regions bounded by the 20 per cent contour of their peak values. From 2D Gaussian fitting (see Section 3.4), we found that the spatial distributions of the emission in all lines are smaller than the MRS (~ 1 arcmin) in ACA observations. In addition, except HCN and HCO^+ , the other lines have FWHM angular sizes smaller than 20 arcsec, suggesting that 12-m-array observations with MRS ~ 20 arcsec could recover most of the line flux.

In a companion work (Liu et al. 2020), we report studies of the star formation scaling relationships between the total bolometric emission (L_{bol} or L_{TIR}) and the molecular line luminosities of $J = 1-0$ transitions of $H^{13}CN$, $H^{13}CO^+$, HCN, and HCO^+ with data obtained from ACA observations for the whole ATOMS sample. We found that both main lines and isotopologue lines can well reveal the total masses of dense gas in Galactic molecular clumps.

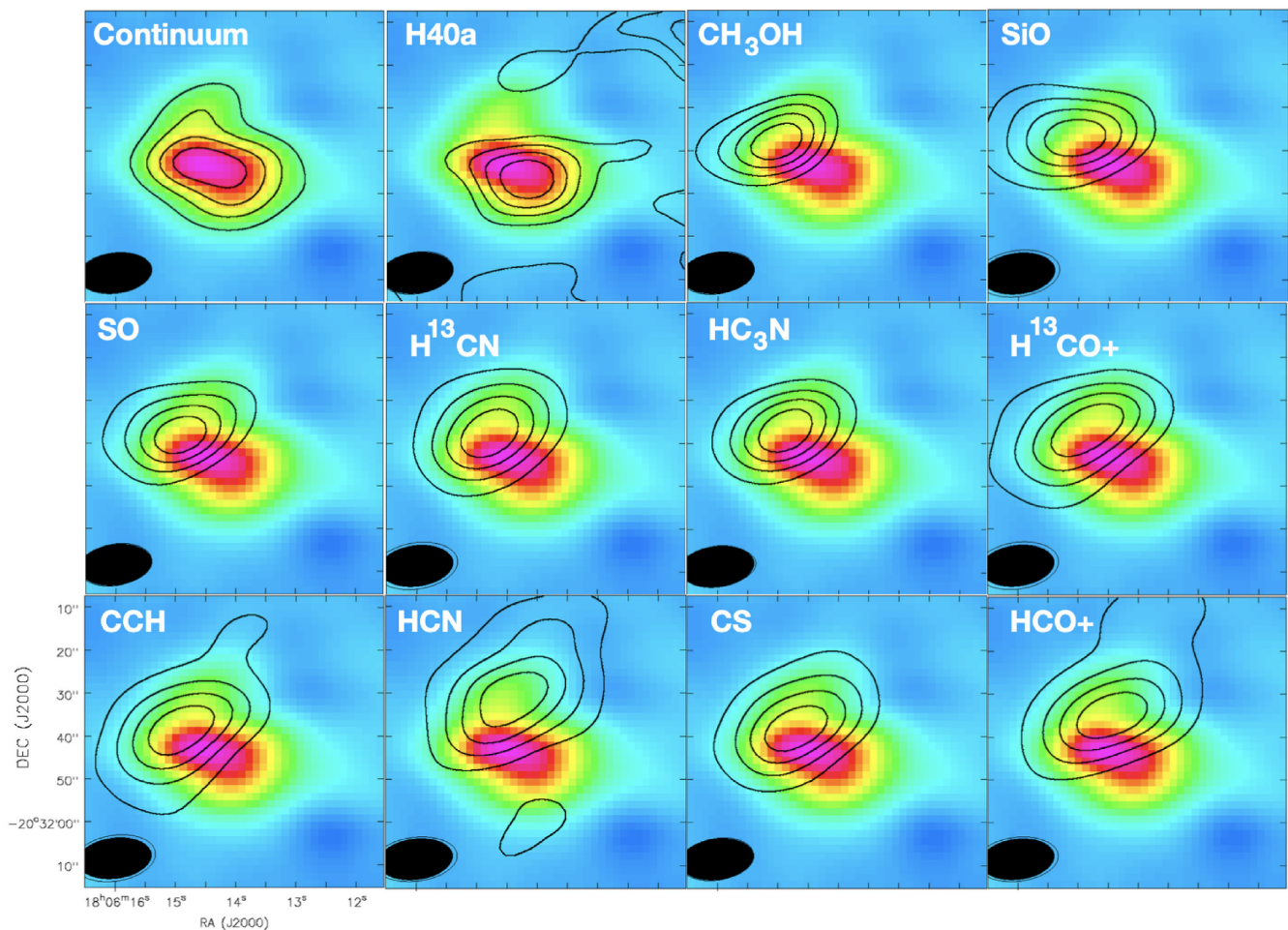


Figure 7. The integrated intensity maps from the ACA images of molecular line emission in G9.62+0.19 are shown in contours. The background colour image is the 3-mm continuum emission. The contour levels are $[0.2, 0.4, 0.6, 0.8] \times F_{\text{peak}}$. The F_{peak} for various tracers are: continuum: $0.225 \text{ Jy beam}^{-1}$; $\text{H}_{40\alpha}$: $7.8 \text{ Jy beam}^{-1} \text{ km s}^{-1}$; CH_3OH : $10.3 \text{ Jy beam}^{-1} \text{ km s}^{-1}$; SiO : $10.3 \text{ Jy beam}^{-1} \text{ km s}^{-1}$; SO : $28.8 \text{ Jy beam}^{-1} \text{ km s}^{-1}$; H^{13}CN : $15.3 \text{ Jy beam}^{-1} \text{ km s}^{-1}$; HC_3N : $34.5 \text{ Jy beam}^{-1} \text{ km s}^{-1}$; H^{13}CO^+ : $15.0 \text{ Jy beam}^{-1} \text{ km s}^{-1}$; CCH : $13.0 \text{ Jy beam}^{-1} \text{ km s}^{-1}$; HCN : $12.1 \text{ Jy beam}^{-1} \text{ km s}^{-1}$; CS : $53.9 \text{ Jy beam}^{-1} \text{ km s}^{-1}$; HCO^+ : $23.6 \text{ Jy beam}^{-1} \text{ km s}^{-1}$.

However, although they are all good tracers of total masses of dense gas, their spatial distributions may be different. The upper panel of Fig. 8 shows the 3-mm continuum emission in colour-scale overlaid with H^{13}CO^+ integrated intensity map in contours. The emission peaks of various gas tracers as revealed in the ACA observations of G9.62+0.19 are marked on this plot. The emission peaks of most gas tracers (except HCN , HCO^+ , and $\text{H}_{40\alpha}$) are close to the H^{13}CO^+ emission peak. The ionized gas traced by $\text{H}_{40\alpha}$ is well associated with the 3-mm continuum emission but is clearly offset from molecular gas and peaks to the south-west. The emission peaks of HCN and HCO^+ are located to the north-west of the H^{13}CO^+ emission peak, indicating that the main lines may show different spatial distributions from their isotopologue lines. The detailed spatial distributions of various gas tracers can be investigated with the high-resolution 12-m-array data.

3.2.2 Moment maps in 12-m-array observations

In the lower panel of Fig. 8, we compare the H^{13}CO^+ spectra from ACA and 12-m-array observations. The spectra that were averaged

over 30-arcsec region centred at the emission peak are nearly identical in both observations. The 12-m-array observation recovers more than 92 per cent of H^{13}CO^+ flux in ACA observations. From Gaussian fits to the spectra, we find a systemic velocity of $\sim 4 \text{ km s}^{-1}$. The linewidth is about 5 km s^{-1} . To compare the spatial distributions of various gas tracers (see Table 2) revealed in 12-m-array observations, we integrate their intensity in the same velocity interval that is from 1.5 to 6.5 km s^{-1} above a threshold of 3σ . This velocity interval is chosen based on the linewidth of H^{13}CO^+ to avoid contamination from outflow emission. In Figs A1, A2, and A3, their integrated intensity (Moment 0) maps (left-hand panels), intensity-weighted velocity (Moment 1) maps (middle panels), and intensity-weighted velocity dispersion (Moment 2) maps (right-hand panels) are presented as colour images. The moment maps were constructed from the data after imposing a cutoff of 3σ . The 3-mm continuum emission is shown as contours on the moment 0 maps for comparison. The contours on moments 1 and 2 maps are showing the integrated intensity maps of corresponding line emission. Below, we will discuss the detailed spatial distributions of various gas tracers based on these maps.

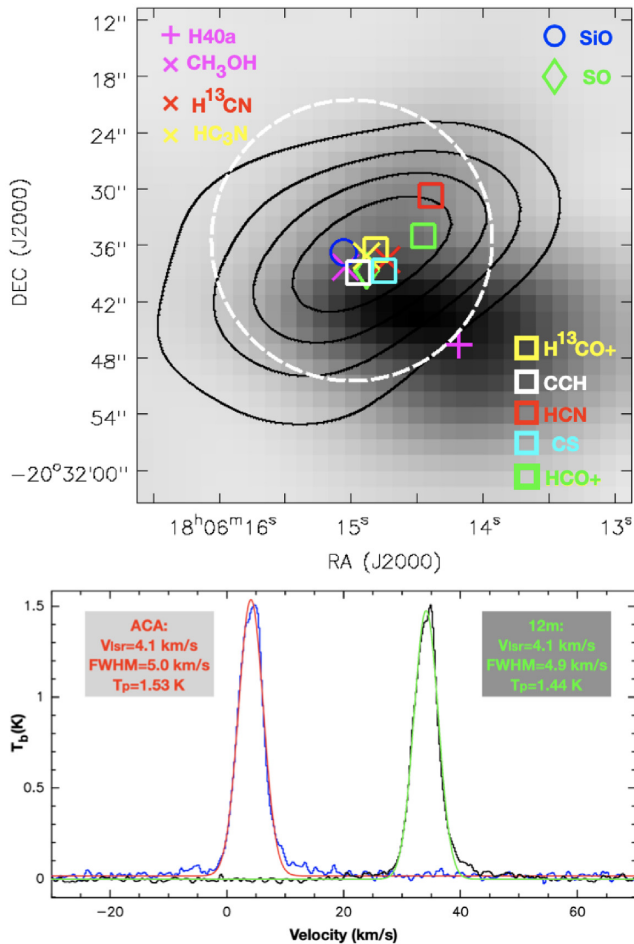


Figure 8. (a) The 3-mm continuum emission of G9.62+0.19 in ACA observations is shown as the grey scale. The integrated intensity from 1.5 to 6.5 km s⁻¹ of H¹³CO⁺ is shown as contours at levels of [0.2, 0.4, 0.6, 0.8] × 15 Jy beam⁻¹ km s⁻¹. The peak positions of various gas tracers of G9.62+0.19 derived from ACA observations are marked with different symbols. (b) The H¹³CO⁺ spectra from the 12-m array and ACA averaged over a 30-arcsec-diameter region (white dashed circle in panel a) are displayed in blue and black, respectively. The spectrum from 12-m-array data is shifted by 30 km s⁻¹. The red and green curves are Gaussian fits. The results of Gaussian fits are also displayed on the panel.

3.2.3 Extended gas emission

CS, HCN, and HCO⁺ are commonly said to be dense gas tracers used in determinations of dense gas star formation laws (Gao & Solomon 2004; Wu et al. 2005, 2010), but this is not always true (Kauffmann et al. 2017; Pety et al. 2017; Shimajiri et al. 2017). As shown in Fig. A1, all the three tracers show very extended emission in the G9.62+0.19 complex. They are poor tracers of the massive filament, where new high-mass stars are forming. Due to large optical depths or absorption, their moment 1 and 2 maps are very complicated and do not show any clear pattern. HCN emission reveals a dense shell-like structure with its emission peak at the position ‘MM4/E’. What we have learned here is that opaque tracers will fail to trace the locations of densest gas on small scales (~0.1 pc) though they are sort of fine to reveal the overall dense gas distribution on larger scales (~1 pc; see Fig. 7).

Besides these main lines with low effective excitation densities ($n_{\text{eff}} < 5 \times 10^3 \text{ cm}^{-3}$), the lines with higher effective excitation

densities ($n_{\text{eff}} > 1 \times 10^4 \text{ cm}^{-3}$) in Table 2 including the isotopologue lines (H¹³CO⁺, H¹³CN) also show widespread emission (see Figs A2 and A3). Interestingly, the H II region ‘B’ appears to have produced a cavity in the molecular clump, which is clearly seen in CCH, H¹³CO⁺, H¹³CN, SO, and HC₃N emission. The H II region ‘B’ is bounded by molecular line emission. H¹³CN emission and 3-mm continuum emission together define a nearly circular region that has a radius of ~0.5 pc, as shown by the magenta dashed circles in Figs A1, A2, and A3. It seems that all high-mass stars in G9.62+0.19 are formed within this 1 pc size natal clump. The Moment 1 maps of these molecular line emission show a clear velocity gradient in the south-west to north-east direction. The gas close to the H II region ‘B’ shows higher redshifted emission. Away from the H II region ‘B’, the gas radial velocity decreases. Line profiles closer to the boundary of the H II region ‘B’ are more redshifted, indicating that the H II region ‘B’ is expanding into its surrounding molecular gas and is reshaping its natal clump.

3.2.4 Tracers for photodissociation regions

CCH is a good tracer of photodissociation regions (PDRs; Pety et al. 2005; Tiwari et al. 2019). In PDRs, the fragmentation of polycyclic aromatic hydrocarbons (PAHs) due to FUV radiation (Le Page, Snow & Bierbaum 2003; Pety et al. 2005; Montillaud, Joblin & Toubanc 2013) or new gas-phase formation routes (Cuadrado et al. 2015) facilitated by heating from high UV flux ($G_0 \sim 10^4 - 10^5$ in Habing units) could give rise to a rich hydrocarbon chemistry. However, CCH emission is widespread in the G9.62+0.19. As shown in Fig. A2, the CCH emission shows a morphology remarkably similar to that of the H¹³CO⁺ emission. It indicates that CCH emission inside massive clumps is not only concentrated in PDRs but is almost omnipresent. CCH has been detected in both nearby dark clouds (Pratap et al. 1997) and distant high-mass star-forming clumps (Beuther et al. 2008; Sanhueza et al. 2012). CCH is produced quickly early on and gets replenished at the clump surfaces by the UV photodissociation of CO (Beuther et al. 2008), leading to its widespread emission in clouds.

HCO⁺ is more easily recombined with free electrons and its abundance is sensitive to the ionization degree of molecular gas. In far-UV irradiated environments (PDRs), its abundances may decrease. Fig. 9(a) presents the CCH-to-H¹³CO⁺ integrated intensity ratio map. In the interface between the H II region ‘B’ and the massive filament, the CCH-to-H¹³CO⁺ intensity ratio is enhanced by a factor of 2–5 when compared to the massive filament itself and its surrounding regions. The enhanced CCH-to-H¹³CO⁺ intensity ratio is likely caused by the PDR of the H II region ‘B’. The H¹³CN-to-H¹³CO⁺ ratio is also enhanced in this thin layer, as seen in Fig. 9(b). High HCN-to-HCO⁺ ratios have also been found in far-UV irradiated environments such as evolved Galactic H II regions (Nguyen-Luong et al. 2020), AGNs (Aladro et al. 2015), or luminous infrared galaxies (LIRGs; Papadopoulos 2007). Therefore, it implies that the high CCH-to-H¹³CO⁺ and H¹³CN-to-H¹³CO⁺ ratios are good tracers of PDRs.

In the ATOMS survey, we will reveal the PDRs utilizing the CCH-to-H¹³CO⁺ and H¹³CN-to-H¹³CO⁺ ratios. We will systematically investigate the chemistry and structure of PDRs (e.g. Goicoechea, Pety & Cuadrado 2016). In particular, we will study how PDRs interact with their natal molecular clumps. In the G9.62+0.19 complex, the PDR of the H II region ‘B’ is clearly interacting with its molecular clump as indicated by the velocity gradients in Moment

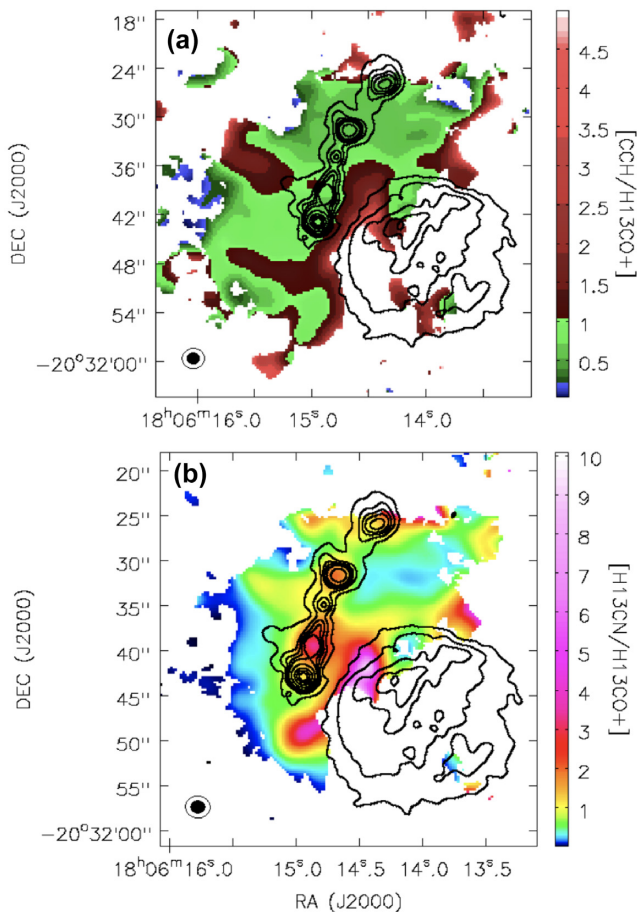


Figure 9. Integrated intensity ratio maps of G9.62+0.19. The contours show the 3-mm continuum emission. Contour levels are the same as in Fig. 5. (a) CCH-to- H^{13}CO^+ ratio; (b) H^{13}CN -to- H^{13}CO^+ ratio.

1 maps of CCH, H^{13}CO^+ , H^{13}CN , SO, and HC_3N emission (see Figs A2 and A3).

3.2.5 Widespread shocked gas emission

In the ATOMS survey, several shock tracers, e.g. SO, SiO, and CH_3OH , are observed and will be used to trace the shocked gas emission. As shown in Fig. A2, SiO emission is widespread in the G9.62+0.19 region. Within the 20 per cent contour in its integrated intensity map, SiO emission shows a large velocity dispersion ($\sigma > 1.5 \text{ km s}^{-1}$), which is mainly related to outflows. However, in more extended regions, i.e. outside the 20 per cent contour in integrated intensity map, SiO emission has a much smaller velocity dispersion of $< 1 \text{ km s}^{-1}$. In Fig. 10, we present the Moment 2 map of SiO emission in the upper left-hand panel and plot the SiO spectra at nine positions of G9.62+0.19 region in other panels. The SiO spectra were obtained by averaging over 5-arcsec area at each position. At positions 5 and 6, SiO shows broad line emission with high-velocity wings, indicating that SiO in these regions is affected by outflow shocks. At other positions, however, SiO emission has much narrower linewidths. We fit the spectra with Gaussian profiles and the results (peak intensity I_p , systemic velocity V_{lsr} and linewidth FWHM) from Gaussian fits of the spectra are summarized in Table 4. The positions 1–4 are located close to H II regions (‘B’, ‘MM1/C’, ‘MM4/E’) and SiO could be excited by H II region shocks. Positions

7–9 are away from both outflows and H II regions. SiO emission at these positions may be caused by other mechanisms, e.g. shocks from large-scale colliding flows. Spectra at positions 1, 4, and 9 can be well fitted with a single Gaussian profile, while spectra at positions 2, 3, 7, and 8 are better fitted with two Gaussians including one narrow component and one broad component. The linewidths of the narrow components range from 2 to 6 km s^{-1} . Widespread, narrow SiO emission has been detected in IRDCs (Jiménez-Serra et al. 2010; Cosentino et al. 2018, 2019) and high-mass protocluster forming regions (Nguyen-Lu’o’ng et al. 2013; Louvet et al. 2016). Such narrow SiO emission can be reproduced by low-velocity shocks in the range 7 to 12 km s^{-1} (Louvet et al. 2016). Such low-velocity shocks are usually attributed to colliding flows or cloud–cloud collision (Jiménez-Serra et al. 2010; Nguyen-Lu’o’ng et al. 2013; Louvet et al. 2016; Moscadelli et al. 2018). We noticed that the narrow components of SiO spectra at positions 7 and 8 are clearly redshifted and blueshifted by $\sim 2\text{--}3 \text{ km s}^{-1}$ from the systemic velocity (4 km s^{-1} measured from H^{13}CO^+) with a projected velocity difference of $\sim 5 \text{ km s}^{-1}$, while the wider components of SiO spectra at positions 7 and 8 are redshifted and blueshifted by $\sim 7\text{--}9 \text{ km s}^{-1}$ from the systemic velocity with a projected velocity difference of $\sim 16 \text{ km s}^{-1}$. This velocity difference indicates that the two elongated structures associated with positions 7 and 8 could be related to large-scale colliding flows that induce low-velocity shocks.

CH_3OH and SO may also trace shocked gas. The upper six panels of Fig. A3 present the moment maps for CH_3OH and SO. In outflow regions, CH_3OH and SO emission show a large velocity dispersion, indicating that they also trace outflow shocks. Beyond the outflow and filament regions, however, the velocity dispersion of CH_3OH and SO is as small ($< 1 \text{ km s}^{-1}$) as that of SiO, suggesting CH_3OH and SO may also trace widespread low-velocity shocks generated from either large-scale colliding flows or H II regions. Widespread CH_3OH emission that may have originated in a large-scale shock interaction has also been detected in IRDCs (Cosentino et al. 2018). However, CH_3OH and SO emission can not only be induced by shocks but also be excited due to pure gas-chemistry in cold cores (Spezzano, Caselli & Bizzocchi 2017; Nagy et al. 2019) or hot cores (Esplagues, Tercero & Cernicharo 2013; Qin et al. 2015). Indeed, they reveal well the dense cores in G9.62+0.19 too (see Section 3.2.6).

In the ATOMS survey, we will for the first time investigate statistically the origin of various velocity shocks in a large sample of massive clumps.

3.2.6 Gas emission tracing dense cores

Fig. A3 presents moment maps of four gas tracers, CH_3OH , SO, H^{13}CN , and HC_3N . All of them trace well the dense cores in the massive filament as identified by the 3-mm continuum emission. H^{13}CN and HC_3N have very similar morphologies. Within the 20 per cent contours in their integrated intensity maps, their morphology is quite similar to that of the 3-mm continuum emission. When compared with other gas tracers in Table 2, these four molecular line transitions seem to be better tracers of dense cores as well as tracers of the massive filament. Their emission maps agree with the 3-mm continuum more than the maps of HCN and HCO^+ .

3.2.7 Outflow gas emission

Several gas tracers in the ATOMS survey, including SiO, SO, CS, HCN, HCO^+ , and CH_3OH , can trace outflows. Here, we

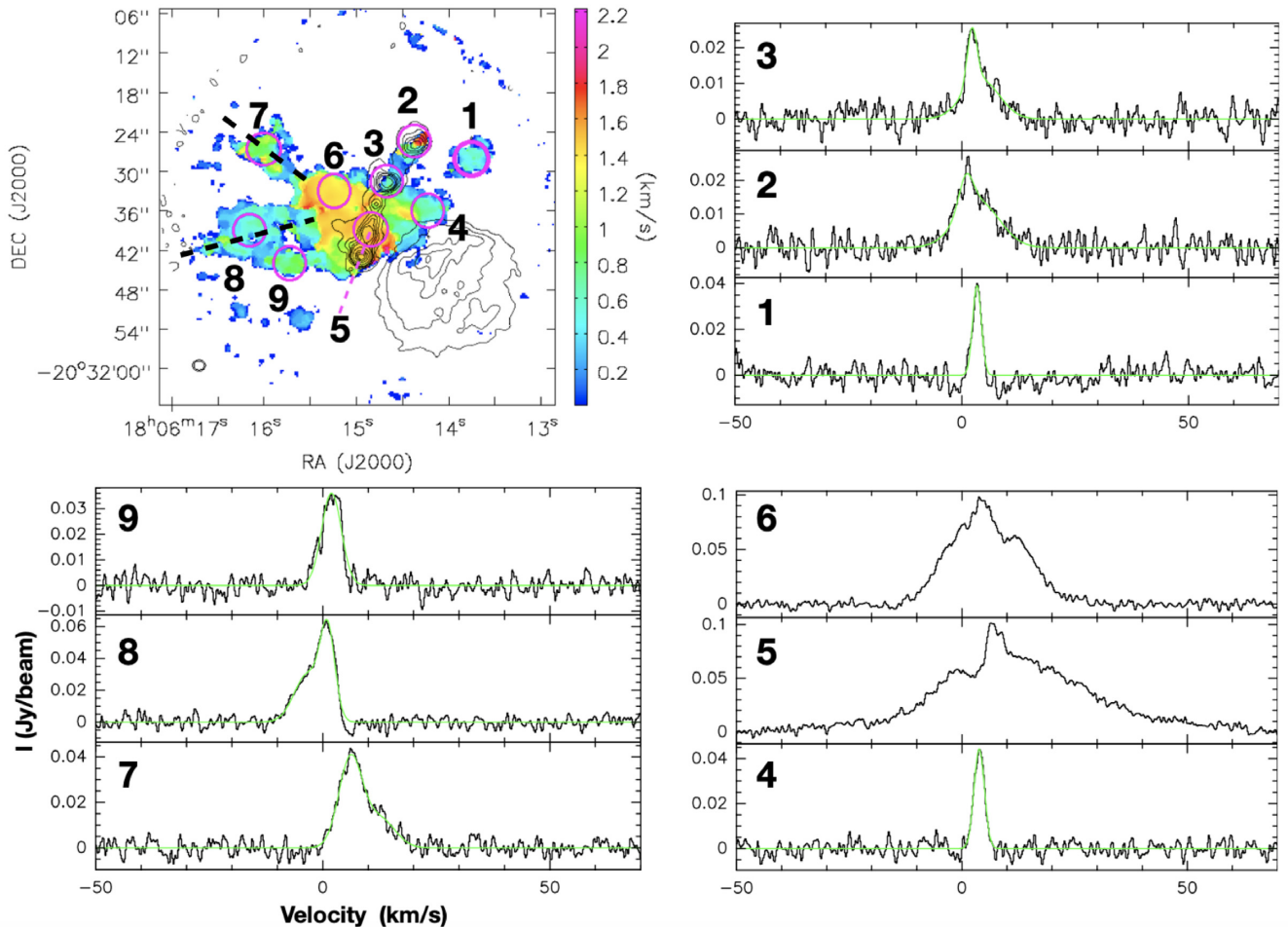


Figure 10. SiO spectra averaged over 5-arcsec regions at nine positions across G9.62+0.19. The upper left-hand panel shows the Moment 2 map of SiO overlaid on 3-mm continuum emission contours. The contour levels are the same as in Fig. 5. The magenta circles mark the positions where the SiO spectra are extracted. The two black dashed lines mark the elongated structures that may be related to colliding flows. The other panels show the averaged SiO spectra at each position. The green lines are Gaussian fits.

demonstrate that the ATOMS data are very useful for identifying protostellar outflows. In Fig. 11, we present the redshifted and blueshifted high-velocity emission of these tracers. The HCN line has three hyper-fine components. To avoid contamination of hyperfine component emission from dense cores, the velocity intervals for redshifted and blueshifted high-velocity emission of HCN are $[20, 50]$ and $[-42, -8]$ km s^{-1} , respectively. For the other tracers, the velocity intervals for redshifted and blueshifted high-velocity emission are $[9, 50]$ and $[-42, -1]$ km s^{-1} , respectively. CH_3OH traces part of the high-velocity outflows driven by the hot core MM8/F, but does not trace the high-velocity outflows driven by the young HMPO MM6 (Liu et al. 2017). The other five outflow tracers reveal the high-velocity outflows driven by both MM8/F and MM6. They show similar outflow morphologies. The outflow properties in G9.62+0.19 have been discussed in detail in Liu et al. (2017). In this paper, we will not further analyse the outflows.

3.2.8 Chemical differentiation among dense cores

The ATOMS survey covers a wide frequency range that includes many molecular transitions in the upper side-band. Fig. 12 presents

the observed spectra (in black) at the emission peak of G9.62+0.19 core MM8/F overlaid with simulated spectra (in red) from XCLASS (eXtended CASA Line Analysis Software Suite; Möller, Endres & Schilke 2017). Several tens of molecular line transitions were identified toward MM8/F. Hence, the ATOMS data are very useful for studying the chemical properties of dense cores. We will identify spectral line transitions using XCLASS, which takes the beam dilution, the line opacity, and line blending into account to identify and simulate the observed molecular line transitions under the assumption of local thermodynamical equilibrium (LTE). XCLASS has been widely used in chemistry studies in the ALMA era (e.g. Allen et al. 2017; Peng et al. 2017, 2019; Pols et al. 2018). The detailed chemical analysis in G9.62+0.19 is beyond the scope of this paper and will be presented in a forthcoming paper (Peng et al., in preparation).

The ATOMS survey data are also very useful for studying chemical differentiation among dense cores that are at different evolutionary stages. Fig. 13 compares the spectra of the two wide SPWs at the positions of six cores in G9.62+0.19. Chemical differentiation is clear among these cores. The cometary H II region ‘B’ is the most evolved source in G9.62+0.19 that has ionized its gas and shows no molecular gas emission. MM1/C is also a cometary

Table 4. Parameters of SiO lines toward G9.62+0.19.

Position	I_p (mJy beam ⁻¹)	V_{lsr} (km s ⁻¹)	FWHM (km s ⁻¹)
1	39	3.38(0.05)	2.25(0.10)
2	10	0.94(0.25)	3.70(0.93)
	14	3.53(0.49)	11.18(0.64)
3	16	2.29(0.10)	2.53(0.25)
	11	4.21(0.30)	9.55(0.77)
4	44	3.87(0.03)	2.73(0.08)
7	39	6.12(0.19)	6.12(0.27)
	13	12.62(0.82)	7.78(1.36)
8	30	-3.30(0.22)	6.97(0.30)
	54	1.07(0.06)	3.80(0.11)
9	36	1.92(0.06)	5.13(0.14)

H II region but is younger than ‘B’. Some strong molecular lines such as HC₃N, SO, and CS are detected toward it. MM11/D is a UC H II region, which shows strong H_{40 α} emission. The molecular line emission toward MM11/D is also much stronger than the corresponding emission toward MM1/C. Cores MM4/E, MM7/G, and MM8/F show typical hot core chemistry with line forests in the two wide bands. MM8/F is associated with energetic outflows and has the richest line emission. MM7/G is also an outflow source but may be still at an earlier evolutionary stage than MM8/F (Liu et al. 2017). Its line emission is much weaker than that of MM8/F. MM4/E is an HC H II region and is not associated with outflows (Liu et al. 2017). Its molecular line emission is also weaker than MM8/F. MM6 is the youngest HMPO in this region that is driving an energetic bipolar outflow, and has not shown hot core chemistry.

Here, we simply demonstrate that the ATOMS data are very useful for studying chemical differentiation among dense cores. In future, we will systematically investigate how the chemistry of dense cores changes with other physical properties like temperature, density, luminosity, and Galactic environments.

3.3 Similarities and differences in the spatial distributions of gas tracers

Due to their different excitation conditions and abundances, different molecular line transitions may trace various physical conditions within molecular clouds, such as density, chemistry, temperature, UV radiation, and so on. Through studying the similarities and differences in the spatial distributions of various gas tracers, we could figure out the best tracers for different structures inside molecular clouds, e.g. filaments, dense cores, and extended cloud envelopes. In the ATOMS survey, we will mainly apply the principal component analysis (PCA; e.g. Lo et al. 2009; Jones et al. 2012, 2013) and histogram of oriented gradients (HOGs; e.g. Soler et al. 2019) analysis methods for this purpose. Below, we will introduce the use of these two methods from the case study of G9.62+0.19.

3.3.1 Principal component analysis

The PCA is a statistical procedure to convert a set of observations of possibly correlated variables into a set of values of linearly uncorrelated variables called principal components (PCs). PCA has been widely used to identify and quantify similarities and differences between various molecular line emission inside molecular clouds (Lo et al. 2009; Jones et al. 2012, 2013; Spezzano et al. 2017; Nagy et al. 2019). We performed PCA on the integrated

emission maps of various gas tracers to characterize their differences in spatial distribution in the G9.62+0.19 complex following a procedure similar to that adopted in these previous works. The integrated intensity maps we used are presented in Figs A1, A2, and A3. These maps are first smoothed and re-gridded to ensure that they have the same resolution and pixel size. We, then, export their pixel values to SPSS software platform¹ for PCA analysis. Table 5 lists the correlation matrix of the input molecules, the eigenvectors, and the eigenvalues of the PCs. From the correlation matrix, one can see that the four dense-gas tracers (CH₃OH, SO, H¹³CN, and HC₃N) are strongly correlated with each other, with correlation coefficients above 0.8. CCH shows strongest correlation with H¹³CO⁺ with a correlation coefficient of 0.91, indicating that these two molecules have very similar spatial distributions, as also mentioned in Section 3.2.3. CS, HCO⁺, and HCN are also strongly correlated with each other. This is consistent with the integrated intensity maps (Fig. A1), showing that CS, HCO⁺, and HCN have similar large-scale spatial distribution (also see Section 3.2.3). SiO is weakly correlated with most molecules except SO. The correlation coefficient between SiO and SO is \sim 0.8, suggesting that the two molecules trace similar shocked gas at large scale.

Fig. 14 presents eigenvalues for each PC in the PCA analysis. We identified three main PCs (1–3) that have eigenvalues larger than 0.5. These three PCs describe 73.62, 9.40, and 6.22 per cent, respectively, of the variance in the data. They together account for nearly 90 per cent of total variation in the data set. The eigenvectors in PCA analysis describe correlations between the variable and the PCs. A (negative) positive eigenvector indicates the molecule is (anti)correlated with the PC. The larger the value, the stronger the correlation. The eigenvectors of each molecule are listed in the last 10 rows in Table 5. Constructed images of the first three PCs are presented in Fig. 15.

For the first PC (PC 1), all the 10 molecules have large positive eigenvectors (>0.7), suggesting that all 10 molecules are positively correlated with each other on large scales and PC 1 resembles the basis of molecular distribution within the G9.62+0.19 clump, as seen in Fig. 15(a). The PC 1 detects well the dense cores as well as the large-scale extended structures.

Fig. 16 shows the plot of eigenvectors of each molecule in PC 2 and PC 3. From this plot, we roughly classify the 10 molecules into three groups as separated by the two mutually perpendicular dashed lines. The two dashed lines are carefully chosen to ensure that the angles between a pair of eigenvectors in each group are smaller than 90°. The first group includes CS, HCO⁺, HCN, CCH, and H¹³CO⁺, which mainly trace extended gas emission and are poor tracers of dense cores. The third group includes SO, CH₃OH, H¹³CN, and HC₃N, which are dense core tracers. SiO in the second group stands out from other molecules because it mainly traces shocked gas. The first and third groups are clearly anticorrelated in Fig. 16. This division of groups, however, is not strict. For example, although SO and SiO are in different groups, the angle between their eigenvectors is only 48°, indicating that they have high similarities somehow. As discussed before, SiO is strongly correlated with SO because both lines are good shock tracers. SO is assigned to the third group because SO is also tracing dense cores as well as other tracers in the same group.

Different groups are also clearly distinguished in the constructed images of the PC 2 and PC 3 (see Figs 15b and c). The dense

¹<https://www.ibm.com/analytics/spss-statistics-software>

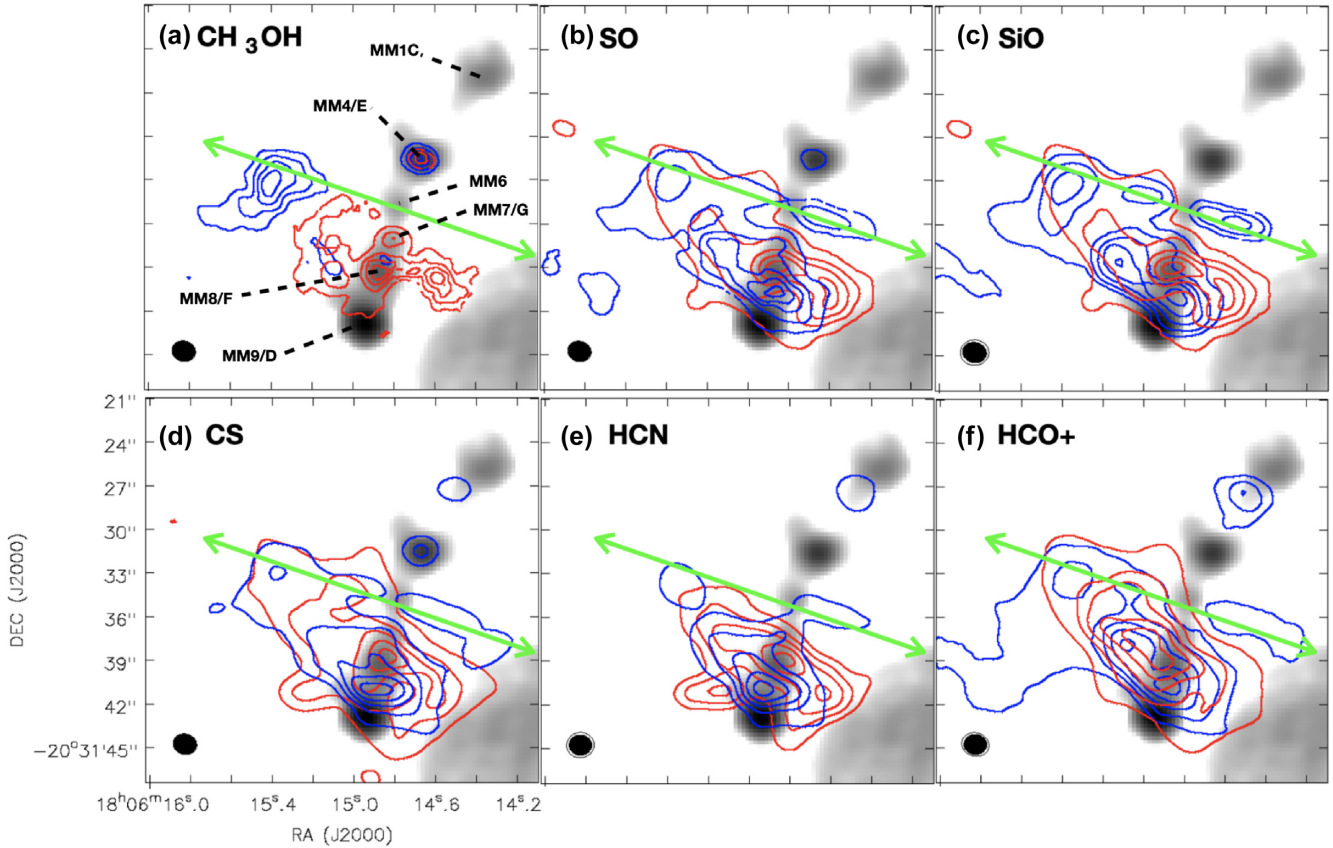


Figure 11. Redshifted and blueshifted high-velocity emission of various gas tracers of G9.62+0.19 are shown in contours. The contours are $[0.1, 0.3, 0.5, 0.7, 0.9] \times F_{\text{peak}}$. The peak integrated intensities (F_{peak}) of CH_3OH blueshifted and redshifted emission are 0.42 and $0.32 \text{ Jy beam}^{-1} \text{ km s}^{-1}$, respectively; F_{peak} of SO blueshifted and redshifted emission are 1.24 and $2.56 \text{ Jy beam}^{-1} \text{ km s}^{-1}$, respectively; F_{peak} of SiO blueshifted and redshifted emission are 1.02 and $2.99 \text{ Jy beam}^{-1} \text{ km s}^{-1}$, respectively; F_{peak} of CS blueshifted and redshifted emission are: 3.89 and $6.6 \text{ Jy beam}^{-1} \text{ km s}^{-1}$, respectively; F_{peak} of HCN blueshifted and redshifted emission are: 5.80 and $3.94 \text{ Jy beam}^{-1} \text{ km s}^{-1}$, respectively; F_{peak} of HCO^+ blueshifted and redshifted emission are 1.72 and $3.41 \text{ Jy beam}^{-1} \text{ km s}^{-1}$, respectively. The green arrow shows the direction of the bipolar outflow driven by MM6 (Liu et al. 2017). The outflows to the south are mainly driven by MM8/F (Liu et al. 2011, 2017). The background image shows the 3-mm continuum emission.

core emission and shocked gas emission are shown in negative contours in the constructed image of the PC 2, while the extended gas emission is shown in solid contours. From the eigenvector plot of the third PC (PC 3 axis of Fig. 16), three molecules (HCN, H^{13}CN , and CH_3OH) show negative eigenvector smaller than -0.2 . They mainly trace dense cores as shown in negative contours in Fig. 15(c). HCN emission is also strongly anticorrelated to PC 3 because its emission is centred on the dense core ‘MM4/E’ in the constructed image of PC 3. H^{13}CO^+ and CCH are strongly correlated with PC 3 with eigenvector larger than ~ 0.2 , while CS and HCO^+ are weakly correlated with PC 3 with eigenvector smaller than ~ 0.1 . It suggests that H^{13}CO^+ and CCH may trace some gas emission structures that are not well traced by CS and HCO^+ (Fig. 15c). Interestingly, we found that H^{13}CO^+ (also CCH) is clearly anticorrelated with H^{13}CN in the PC 2 and PC 3. The angle between their eigenvectors in Fig. 16 is close to 180° , suggesting that they trace very different structures in these two PCs. It is because H^{13}CO^+ and CCH do not trace the dense cores at all, while H^{13}CN emission coincides with the dense core emission very well.

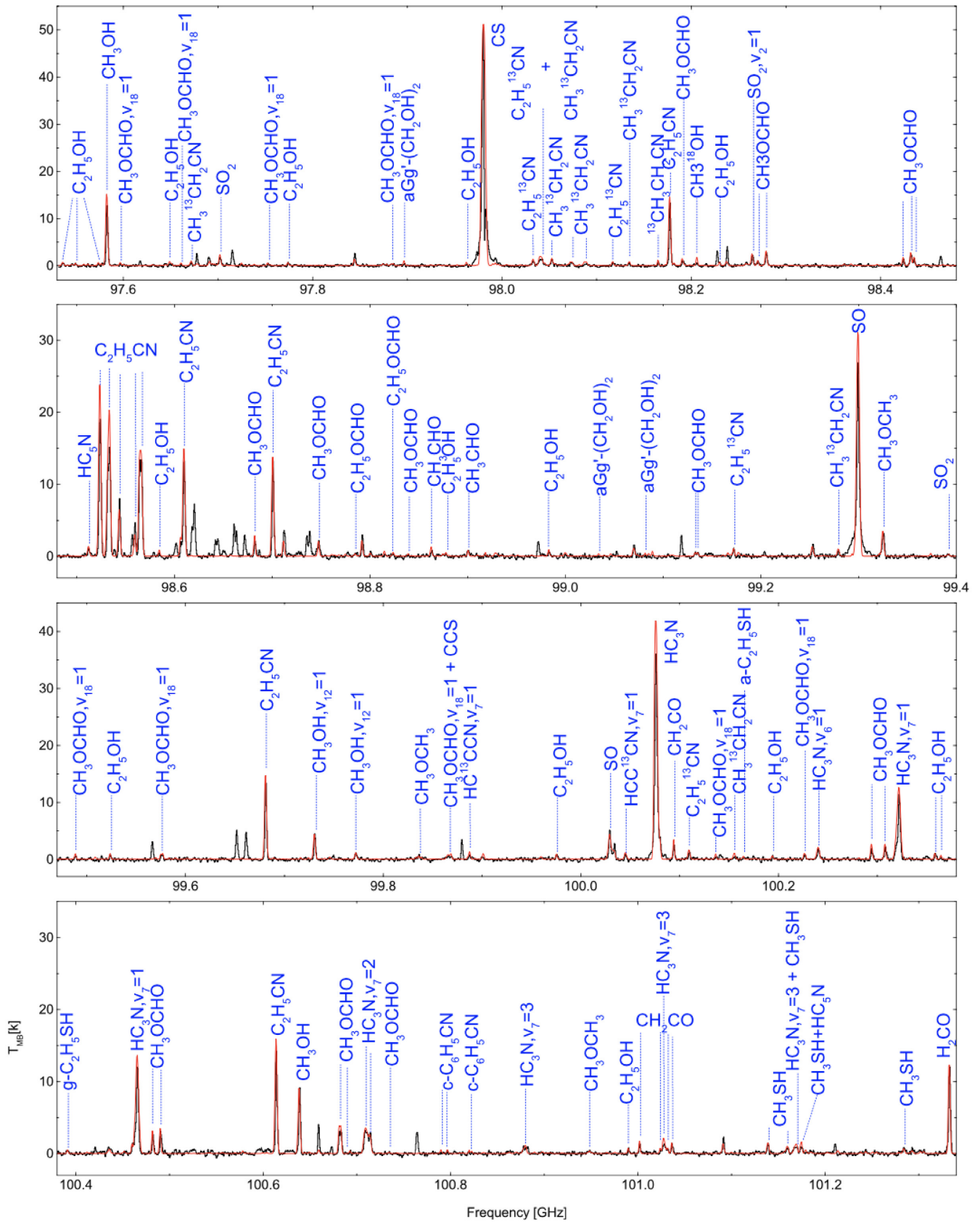
From PCA analysis, we learned that CS, HCO^+ , HCN, CCH, and H^{13}CO^+ show high similarities in spatial distribution because they mainly trace extended gas emission and they are poor tracers of dense cores in G9.62+0.19. In contrast, CH_3OH , H^{13}CN , and HC_3N trace dense cores well. SiO line is a pure shock tracer. It has

high similarity with another shock tracer, SO. However, SO line emission can trace well not only shocked gas but also dense cores. The PCA analysis is very powerful in separating different kinds of gas and will be used in further studies in the ATOMS survey to characterize gas distributions.

3.3.2 Histogram of oriented gradients analysis.

An alternative way to study the spatial correlation between different tracers in molecular clouds is the HOGs analysis (Soler et al. 2019). In the HOGs method, it is assumed that the appearance and shape of an object in an image can be well characterized by the distribution of local intensity gradients or edge directions. The HOG method quantifies similarities and differences in two images by studying the occurrences of the relative orientations between their local gradient orientations. Soler et al. (2019) investigated the spatial correlation of the HI and ^{13}CO , and found a significant spatial correlation between the two tracers in velocity channels where $V_{\text{HI}} \approx V_{^{13}\text{CO}}$.

In this work, we performed a HOGs analysis on the integrated intensity maps of various gas tracers following the procedure in Soler et al. (2019). Three statistical evaluation parameters are derived: mean resultant vector length (r), the projected Rayleigh statistic (V), and the alignment measurement (AM). The definitions



Downloaded from https://academic.oup.com/mnras/article/496/3/2790/5854208 by Universidad de Chile user on 25 November 2020

Figure 12. Sample spectra at the emission peak of G9.62+0.19 core MM8/F. The black curve is the observed spectra, and red curve indicates the simulated spectra with XCLASS. The identified molecular line transitions are labelled.

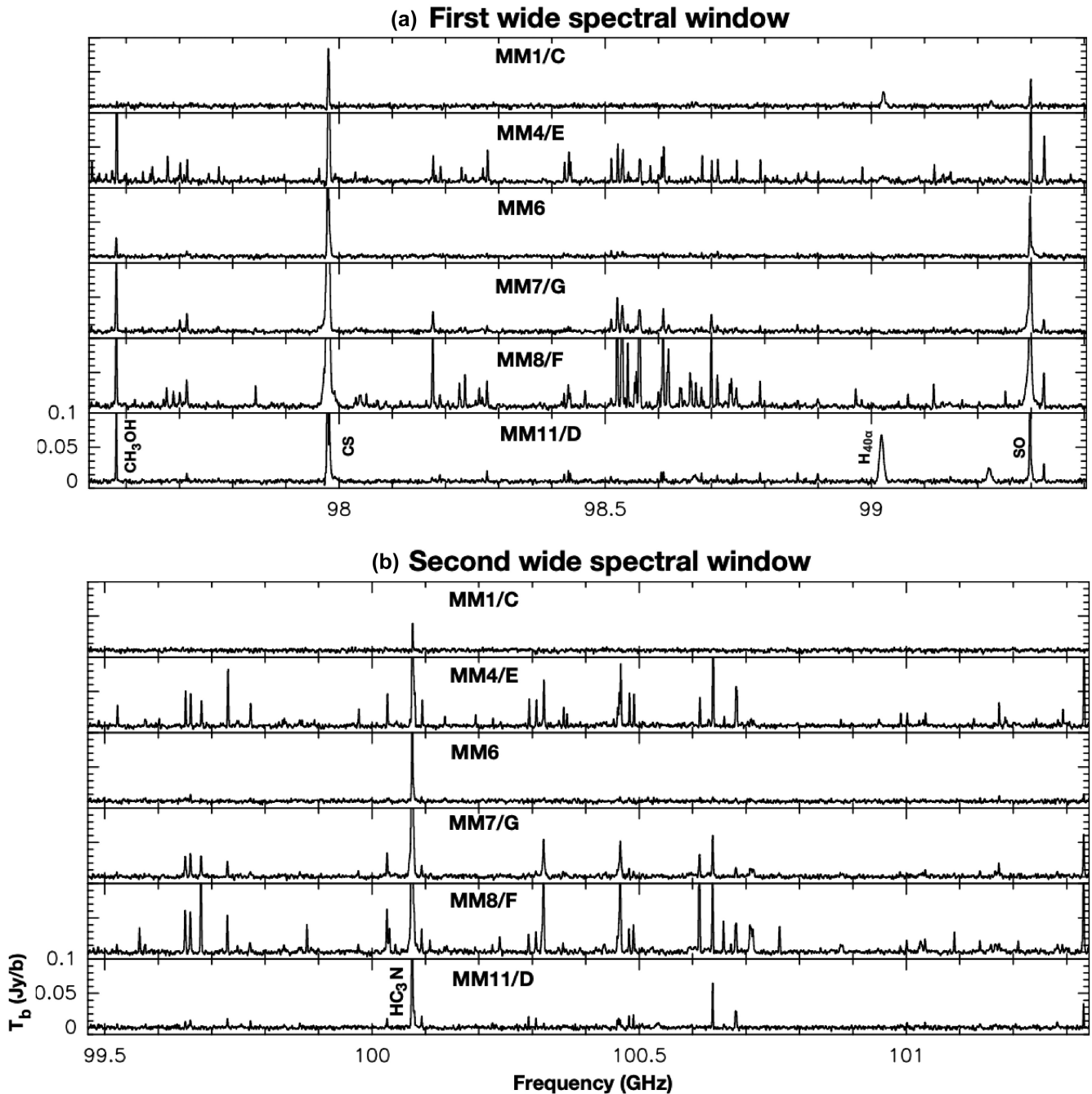


Figure 13. The line spectra of the two wide SPWs averaged over 2 arcsec at each core of G9.62+0.19.

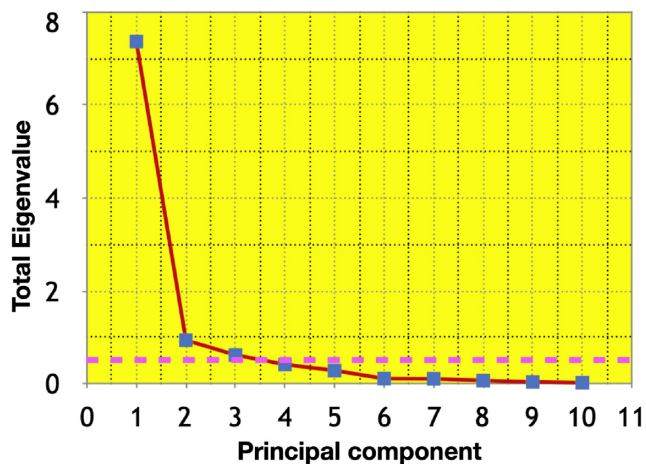
of these parameters are given in Soler et al. (2019). The resultant vector length, r , is a normalized quantity that can be interpreted as the fraction of uniform distribution of angles between gradient vectors. A preferential relative orientation (either parallel or perpendicular) in two images is of statistical significance if r differs from zero significantly. The projected Rayleigh statistic (V) is used to determine whether or not gradient vectors have mostly parallel ($V > 0$) or perpendicular ($V < 0$) relative orientations. The higher the V values, the more similarity in two images. The alignment measurement (AM), is an alternative method for estimating the degree of alignment between vectors (Lazarian & Hoang 2007).

High V and AM values indicate mostly parallel relative orientations between the gradient vectors.

Three statistical evaluation parameters from HOGs analysis are summarized in Table 6. The three parameters give consistent statistical evaluation results. HC_3N is strongly correlated with six molecules (H^{13}CN , H^{13}CO^+ , HCO^+ , CCH , SO , CS), with $r > 0.2$, $V > 1000$, and $\text{AM} > 0.4$. This correlation arises because HC_3N is a good tracer for both dense cores and extended structures (see Fig. A3). The strongest correlation occurs between HC_3N and H^{13}CN with r of 0.43, V of 1770, and AM of 0.61. These two molecules have similar geometry in their integrated intensity

Table 5. PCA analysis of G9.62+0.19.

	CCH	CH ₃ OH	CS	H ¹³ CN	H ¹³ CO ⁺	HC ₃ N	HCN	HCO ⁺	SiO	SO
The correlation matrix of the input molecular dataset										
CCH	1.00	0.56	0.79	0.70	0.91	0.77	0.59	0.73	0.60	0.75
CH ₃ OH	0.56	1.00	0.57	0.83	0.62	0.87	0.48	0.47	0.56	0.84
CS	0.79	0.57	1.00	0.81	0.76	0.75	0.68	0.87	0.57	0.81
H ¹³ CN	0.70	0.83	0.81	1.00	0.75	0.94	0.63	0.70	0.54	0.87
H ¹³ CO ⁺	0.91	0.62	0.76	0.75	1.00	0.83	0.62	0.75	0.60	0.80
HC ₃ N	0.77	0.87	0.75	0.94	0.83	1.00	0.62	0.69	0.66	0.92
HCN	0.59	0.48	0.68	0.63	0.62	0.62	1.00	0.79	0.35	0.60
HCO ⁺	0.73	0.47	0.87	0.70	0.75	0.69	0.79	1.00	0.48	0.71
SiO	0.60	0.56	0.57	0.54	0.60	0.66	0.35	0.48	1.00	0.78
SO	0.75	0.84	0.81	0.87	0.80	0.92	0.60	0.71	0.78	1.00
The eigenvectors and eigenvalues of the principal components										
Component	1	2	3	4	5	6	7	8	9	10
Percentage of variance (%)	73.62	9.40	6.22	4.18	2.89	1.16	1.12	0.72	0.43	0.26
CCH	0.87	0.13	0.27	-0.32	0.09	0.13	0.10	0.10	-0.06	0.02
CH ₃ OH	0.80	-0.45	-0.34	0.00	0.07	-0.02	0.20	0.01	0.07	0.01
CS	0.89	0.25	0.06	0.05	-0.33	0.14	0.05	-0.08	0.06	-0.05
H ¹³ CN	0.91	-0.12	-0.28	-0.07	-0.16	0.05	-0.18	0.07	0.03	0.08
H ¹³ CO ⁺	0.90	0.08	0.18	-0.30	0.16	-0.11	-0.07	-0.13	0.08	0.01
HC ₃ N	0.94	-0.21	-0.14	-0.08	0.04	-0.04	-0.10	0.06	-0.05	-0.12
HCN	0.74	0.47	-0.25	0.26	0.31	0.10	-0.02	-0.02	0.00	0.00
HCO ⁺	0.84	0.44	0.03	0.13	-0.12	-0.23	0.06	0.09	-0.01	0.01
SiO	0.71	-0.36	0.48	0.35	0.07	0.02	-0.05	0.05	0.05	0.01
SO	0.95	-0.22	0.02	0.10	-0.05	-0.03	0.03	-0.14	-0.14	0.04


Figure 14. The eigenvalue against the component number of the 10 principal components (PCs). The dashed line marks an eigenvalue threshold of 0.5.

maps (see Fig. A3). H¹³CO⁺ is most correlated with CCH, as also mentioned in Section 3.2.3. The r , V , and AM values for the pair of H¹³CO⁺ and CCH are 0.33, 2051, and 0.54, respectively. CS shows highest correlation with HCO⁺ with V of 2373 and AM of 0.43, suggesting that they have very similar spatial distributions. HCN shows strongest correlations with CS and HCO⁺ with $V > 800$ and AM > 0.3 . The SiO image is most similar to SO image with V of 1078 and AM of 0.54, suggesting that SiO and SO may reveal similar shocked gas distribution. CH₃OH shows strongest correlations ($V \gtrsim 450$ and $AM \gtrsim 0.45$) with H¹³CN, HC₃N, and SO because they trace similar dense gas distribution in the massive filament.

The HOGs analysis is also consistent with the previous PCA analysis. Molecules in the same group defined by the PCA analysis in Fig. 14 show the strongest correlations in the HOGs analysis.

We also investigate the similarities and differences between the 3-mm continuum emission and gas emission. We only performed HOGs analysis in the massive filament region. For example, the grey image in the upper panel of Fig. 17 shows the absolute values of relative orientation angles (ϕ ; colour image) between the 3-mm continuum map (yellow contours) and the HC₃N map (red contours) in the filament region. The histograms of relative orientation angles between 3-mm continuum and molecules are shown in Figs 17 and 18. From the histograms, one can see that the distributions of relative orientation angles for HC₃N, H¹³CN, CH₃OH, and SO are clearly peaked around 0° with small dispersions. However, the other molecules show much more flat distributions. It indicates that HC₃N, H¹³CN, CH₃OH, and SO are the best to trace the dense structures (filaments and cores) as the 3-mm continuum emission. The other molecules are poor tracers for those dense structures. As shown in Table 6, HC₃N shows highest similarity with the 3-mm continuum emission. The r , V , and AM for the HC₃N and 3-mm continuum correlation are 0.32, 1138, and 0.53, respectively. SiO shows largest difference with the 3-mm continuum emission. The r , V , and AM for the SiO and 3-mm continuum correlation are 0.08, 119, and 0.32, respectively, indicating that SiO cannot trace dense structures at all.

3.4 Fraction of line fluxes from filaments and cores

One of the main science goals of the ATOMS survey is to statistically evaluate what portion of gas in the gravitationally bound clumps is actually participating in star formation or is concentrated in the smallest star formation units, i.e. dense cores. In this section, we explore what fraction of the fluxes of the various lines comes from the massive filament that is forming high-mass stars in G9.62+0.19.

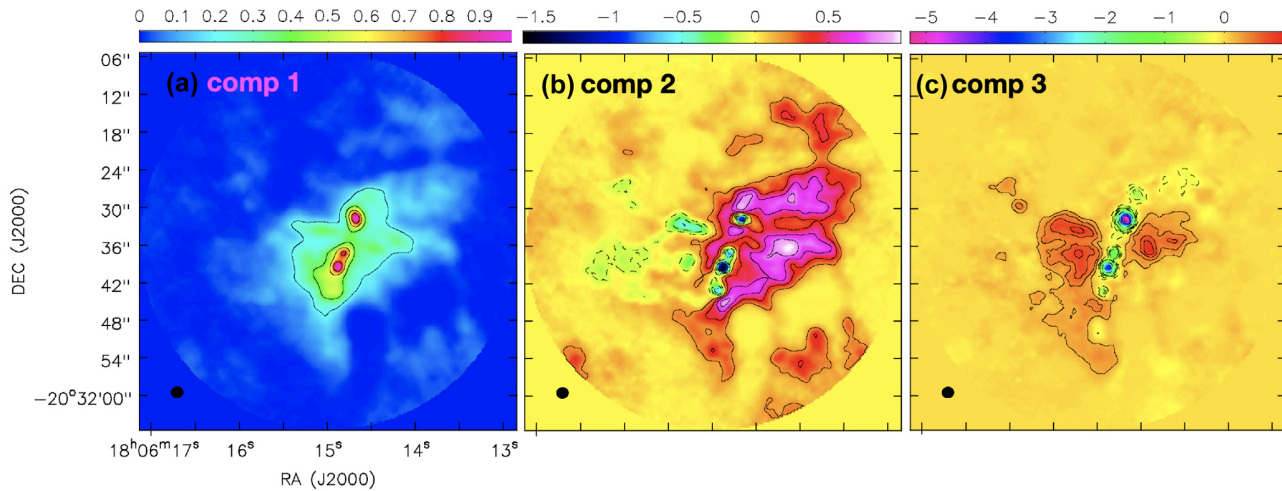


Figure 15. Constructed images of the first three PCs. The images are normalized to their maximum values. (a) PC 1. The contours are 0.2, 0.4, 0.6, 0.8. (b) PC 2. The contours are -1.5 , -1.3 , -1.1 , -0.1 , 0.2, 0.4, 0.6, 0.8. (c) PC 3. The contours are -5 , -4 , -3 , -2 , -1 , -0.8 , -0.6 , -0.4 , -0.2 , 0.2, 0.4, 0.6, 0.8.

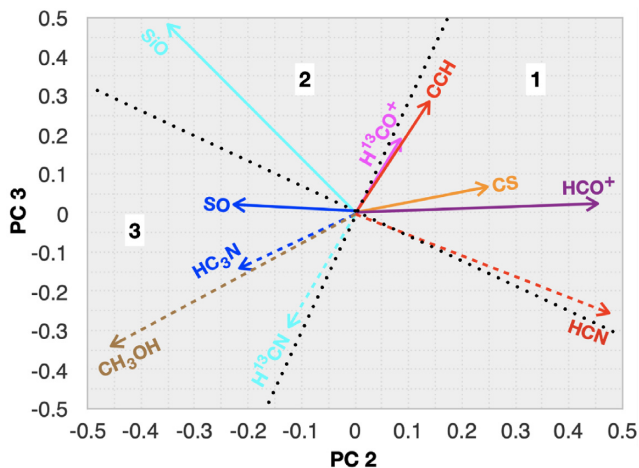


Figure 16. Plots of eigenvectors of the second and third PCs of the data set. Each of the eigenvectors represents the component of that molecule in the relevant PC. The two mutually perpendicular dashed lines separate the molecules into three groups.

In Table 7, we compare the total integrated intensities of various molecular lines obtained from ACA measurements with that obtained from 12-m-array measurements. The integrated intensities are derived in the velocity interval of 1.5 to 6.5 km s⁻¹. The deconvolved FWHM angular sizes, peak integrated intensities, and total integrated intensities (S_v^{ACA}) of various molecular lines in ACA data are derived from a 2D Gaussian fitting, and are listed in columns 2–4 in Table 7. The total integrated intensities ($S_v^{12\text{m}}$) of molecular lines in 12-m-array data are measured within the massive filament region that is bounded by the 1 per cent of peak flux density contour ($\sim 3.5\sigma$ level) of the 3-mm continuum emission. We did not perform 2D Gaussian fitting on 12-m-array data because the massive filament is far from a 2D Gaussian shape. We also did not measure integrated intensities of molecular lines in the H II region ‘B’, because there is no molecular line emission associated with it. The 1 per cent of peak flux density contour of the 3-mm continuum emission defines well the boundary of the massive filament (see Fig. 5). The ratios of $S_v^{12\text{m}}$ to S_v^{ACA} listed in the last column in Table 7 can be used to evaluate how much emission is from the densest filament region.

Fig. 19 shows the ratios against the AM values that are derived from HOGs analysis. There is a clear trend between the ratios and the AM values. Molecules with higher AM values show higher similarity with the 3-mm continuum emission. Molecules (CH₃OH, HC₃N and H¹³CN) that have high AM values also show high ratios of $S_v^{12\text{m}}$ to S_v^{ACA} (> 40 per cent), further suggesting that these molecular lines are good tracers of the dense filament. In contrast, only less than 25 per cent of the fluxes of CCH, HCN, CS, and HCO⁺ are from the dense filament region. These molecules also show largest differences (small AM values) with the spatial distribution of the 3-mm continuum emission.

The G9.62+0.19 is a gravitationally bound massive clump (Liu et al. 2017, 2018c). Molecular lines HCN $J = 1-0$, CS $J = 2-1$ and HCO⁺ $J = 1-0$ are commonly used in dense gas star formation law studies (Gao & Solomon 2004; Wu et al. 2005, 2010). Our studies indicate that even in such a gravitationally bound clump, these commonly used lines are poor tracers of the dense structures, e.g. filament or dense cores. This is consistent with observations in nearby GMCs, where these lines do not well trace the column density structures (cores and filaments) revealed in *Herschel* images (Pety et al. 2017; Shimajiri et al. 2017). Our studies of G9.62+0.19 indicate that the gas lines within the dense filament as defined by the continuum emission only contributes to less than 25 per cent flux of these lines. These main lines of dense gas tracers are poor tracers of dense structures because they tend to be optically thick in dense parts of molecular clouds (e.g. Sanhueza et al. 2012; Hoq et al. 2013; Shimajiri et al. 2017; Liu et al. 2020). The large optical depths of main lines, such as HCN and HCO⁺, indicate that the density or mass estimates from their line intensity could be misleading. In contrast to the main lines, emission from the isotopologues are optically thinner because of their much lower abundances and hence higher effective excitation densities (Shirley 2015). Therefore, they are potentially better tracers of the column densities and dense structures in molecular clouds. The optical depth issues in dense gas star formation law studies with main lines will be discussed in a companion paper by Liu et al. (2020).

In dense gas star formation law studies (e.g. Wu et al. 2010), the line luminosity (L'_{mol}) is assumed as a tracer for dense gas mass (M_{dense}). Wu et al. (2010) found that the median conversion factors from line luminosity to dense gas masses ($L'_{\text{mol-to-}M_{\text{dense}}}$) are about 20, 39, 16, and 19 M_{\odot} (K km⁻¹ pc²)⁻¹ for CS $J = 2-1$, CS $J = 7-6$,

Table 6. HOG analysis of G9.62+0.19.

Lines	Continuum	HC ₃ N	H ¹³ CN	H ¹³ CO ⁺	CCH	CS	HCO ⁺	HCN	SO	CH ₃ OH	SiO
<i>r</i>											
continuum	1.00										
HC ₃ N	0.32	1.00									
H ¹³ CN	0.30	0.43	1.00								
H ¹³ CO ⁺	0.10	0.33	0.16	1.00							
CCH	0.13	0.28	0.18	0.33	1.00						
CS	0.11	0.20	0.29	0.08	0.16	1.00					
HCO ⁺	0.11	0.17	0.21	0.18	0.12	0.19	1.00				
HCN	0.07	0.05	0.11	0.03	0.03	0.08	0.07	1.00			
SO	0.20	0.29	0.29	0.12	0.14	0.19	0.09	0.09	1.00		
CH ₃ OH	0.24	0.26	0.25	0.02	0.03	0.10	0.05	0.08	0.23	1.00	
SiO	0.08	0.15	0.06	0.12	0.07	0.05	0.07	0.04	0.33	0.21	1.00
<i>V</i>											
Continuum	5278										
HC ₃ N	1138	6972									
H ¹³ CN	1040	1770	4707								
H ¹³ CO ⁺	388	1961	712	8011							
CCH	512	1714	774	2051	9193						
CS	571	1334	1387	546	1267	15850					
HCO ⁺	485	1083	964	1278	972	2373	18196				
HCN	317	300	503	−24	179	809	845	16265			
SO	823	1620	1243	764	701	1514	598	554	8115		
CH ₃ OH	391	644	448	28	57	266	90	179	661	2933	
SiO	119	381	119	163	138	169	169	156	1078	452	3354
<i>AM</i>											
Continuum	1.00										
HC ₃ N	0.53	1.00									
H ¹³ CN	0.51	0.61	1.00								
H ¹³ CO ⁺	0.35	0.54	0.41	1.00							
CCH	0.38	0.50	0.42	0.54	1.00						
CS	0.37	0.43	0.51	0.33	0.40	1.00					
HCO ⁺	0.36	0.42	0.44	0.42	0.37	0.43	1.00				
HCN	0.33	0.32	0.37	0.27	0.29	0.33	0.32	1.00			
SO	0.44	0.50	0.50	0.37	0.38	0.43	0.34	0.35	1.00		
CH ₃ OH	0.46	0.46	0.46	0.29	0.30	0.35	0.31	0.34	0.45	1.00	
SiO	0.32	0.38	0.33	0.33	0.31	0.32	0.32	0.30	0.54	0.44	1.00

HCN $J = 1-0$, and HCN $J = 3-2$ lines, respectively. In the ATOMS survey, we are more interested in how the total line luminosity of clumps correlates to the total masses (M_{cores}) of dense cores, i.e. the smallest star formation units. In G9.62+0.19, the total line flux densities of H¹³CN, H¹³CO⁺, HCN, and HCO⁺ that are integrated over all velocity channels in ACA observations are 87, 45, 258, and 176 K km^{−1}, respectively. We can convert the total flux densities of these lines into their line luminosity following Solomon et al. (1997). The line luminosity of the $J = 1-0$ transitions of H¹³CN, H¹³CO⁺, HCN, and HCO⁺ of the G9.62+0.19 clump are 10, 5, 29, and 19 K km^{−1} pc², respectively. Liu et al. (2017) identified 12 dense cores in G9.62+0.19. The total mass of these dense cores is $\sim 400 M_{\odot}$, assuming an average dust temperature of 35 K (Liu et al. 2017). Therefore, the conversion factors $L'_{\text{mol-to-}M_{\text{cores}}}$ in G9.62+0.19 are about 40, 80, 14, and 21 $M_{\odot} (\text{K km}^{-1} \text{pc}^2)^{-1}$ for the $J = 1-0$ transitions of H¹³CN, H¹³CO⁺, HCN, and HCO⁺, respectively. In future, we will statistically investigate the conversion factors of line luminosity to dense core masses with the full ATOMS sample, which is very helpful to investigate how SFE varies across Galactic clumps. The knowledge of these studies can also be applied to star formation in external galaxies.

4 DISCUSSION

4.1 Stellar feedback and sequential high-mass star formation

The ATOMS aims to investigate how stellar feedback from formed OB (proto)stars in protoclusters affect their natal clumps and regulate new star formation. Below, we discuss the stellar feedback effect in G9.62+0.19.

As discussed in Section 3.2.8 and in Liu et al. (2017), sequential high-mass star formation is taking place inside the G9.62+0.19 clump, which has a size of ~ 1 pc. The oldest H II regions in this area seem to have a great influence on their natal clump, creating a cavity in molecular line emission. From moment 1 maps (see middle panels of Figs A2 and A3) of several molecular lines (e.g. CCH, H¹³CO⁺, SO, and HC₃N), one can see clearly a velocity gradient across the clump. Such large-scale velocity gradient and widespread low-velocity SiO shocks surrounding the H II regions are more likely caused by the expansion of the H II region ‘B’. It indicates that stellar feedback from formed OB protostars can greatly reshape their natal clumps and change the spatial distribution of gas.

We also noticed that the evolved OB protostars in G9.62+0.19 are not located near the centre of the clump but are clearly close

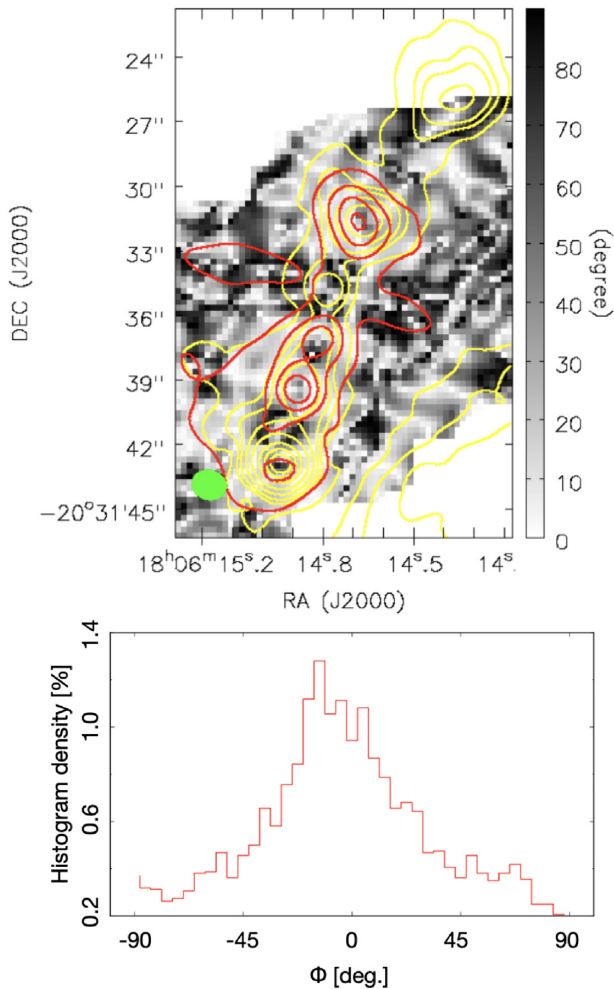


Figure 17. Upper panel: The background image shows the absolute values of relative orientation angles (ϕ) between the 3-mm continuum image and the HC_3N image of G9.62+0.19. The yellow contours show the 3-mm continuum emission. The contour levels are [0.01, 0.03, 0.05, 0.07, 0.1, 0.2, 0.4, 0.6, 0.8] $\times 74.1 \text{ mJy beam}^{-1}$. The HC_3N integrated intensity map is shown in red contours. The contour levels are [0.2, 0.4, 0.6, 0.8] $\times 3.09 \text{ Jy beam}^{-1} \text{ km s}^{-1}$. Lower panel: Histogram of relative orientation angles.

to the clump edges. Along the massive filament, evolved sources are located at the ends and the youngest sources are located in the filament centre. This phenomenon is similar to the ‘edge-collapse’ process proposed for filaments (Pon, Johnstone & Heitsch 2011; Pon et al. 2012; Clarke & Whitworth 2015). For long filaments with aspect ratios larger than 2, the global collapse of the filaments is likely end-dominated (Clarke & Whitworth 2015). The ends experience the highest acceleration, and this leads to the formation of end-clumps, which then converge on the centre. In addition, recent ALMA high-resolution observations of massive IRDCs indicate that there is no significant evidence of primordial mass segregation (Contreras et al. 2018; Sanhueza et al. 2019). More massive cores are distributed in the same way as other low-mass cores (Contreras et al. 2018; Sanhueza et al. 2019). The observations of those IRDCs are consistent with what we have found here in the G9.62+0.19 clump. It seems that high-mass stars are not necessarily formed at the clump centre as expected by the ‘competitive accretion’ model (Bonnell et al. 2002; Bonnell & Bate 2006; Bonnell 2008). Recently, Padoan et al. (2019) proposed a new

scenario of massive-star formation, the ‘Inertial-Inflow Model’, in which massive stars are assembled by large-scale, converging, inertial flows that naturally occur in supersonic turbulence.

Based on our knowledge of the G9.62+0.19 clump and recent studies of IRDCs, we propose the following scenario to explain the sequential high-mass star formation in pc-size clumps. The sketch of the scenario is shown in Fig. 20. The three stages involved in protocluster formation of this scenario are as follows:

(a) The initial fragmentation of a massive clump does not show significant evidence of primordial mass segregation (Sanhueza et al. 2019). The clumps are accreting gas from large-scale converging flows (Padoan et al. 2019). These flows generate low-velocity shocks that excite widespread narrow SiO emission.

(b) As proposed in the ‘edge-collapse’ scenario (Pon et al. 2011, 2012; Clarke & Whitworth 2015), dense cores that are near the clump edges or at the ends of dense filaments inside clumps have higher accretion rates and are more gravitationally unstable. They will be the first to collapse to form protostars. Dense cores and formed protostars keep accreting gas from clump gas. High-mass protostars could form away from clump centre as seen in the G9.62+0.19 complex.

(c) Stellar feedback from formed OB stars reshapes their natal clumps and changes the spatial distribution of gas and dense cores. The expansion of H II regions can also generate low-velocity shocks that excite widespread narrow SiO emission in their surroundings. Some low-mass dense cores could be destroyed as H II regions expand into the clump. Some dense cores in front of H II regions may collide and merge into massive cores or massive filament due to the enhanced density by the H II region shocks. This can explain the lack of widespread low-mass cores in the G9.62+0.19 complex (Liu et al. 2017). New generation of high-mass protostars could form in these new massive cores.

Statistical studies of a large number of protoclusters in the ATOMS survey will help test this scenario.

4.2 Links to other surveys

There are several on-going or completed survey programmes aiming at studying dense gas in either Galactic GMCs or external galaxies. In this section, we will introduce several of these surveys and discuss how they will connect to the ATOMS survey.

The ‘Millimetre Astronomy Legacy Team 90 GHz (MALT90)’ survey (PI: J. M. Jackson) has used the Mopra 22-m single-dish telescope to obtain $3 \times 3 \text{ arcmin}^2$ maps in various gas tracers towards ~ 2000 dense molecular clumps that are at different evolutionary stages (Sanhueza et al. 2012; Jackson, Rathborne & Foster 2013; Stephens et al. 2016). The MALT90 project aims to characterize the physical and chemical evolution of high-mass star-forming clumps. The ATOMS survey observed similar gas tracers as in the MALT90 project, e.g. HCN, HCO^+ , and their isotopologue lines, CCH, SiO, and HC_3N . The ATOMS survey data will be used to study the star formation scaling relations (Liu et al. 2020), and compared with those derived using MALT90 data (Stephens et al. 2016). The ATOMS survey has a much higher angular resolution (2 versus 38 arcsec) than the MALT90 project. The ATOMS survey will reveal the internal structures and detailed spatial gas distributions within the Galactic clumps that cannot be resolved in the MALT90 project.

The ‘Orion B: The Anatomy of a GMC’ (PI: J. Pety) is a multiline imaging survey at the IRAM 30-m telescope toward the Orion B molecular cloud (Pety et al. 2017). It covers approximately thirty 3-mm lines with a typical resolution of 26 arcsec (or $\sim 0.05 \text{ pc}$ at

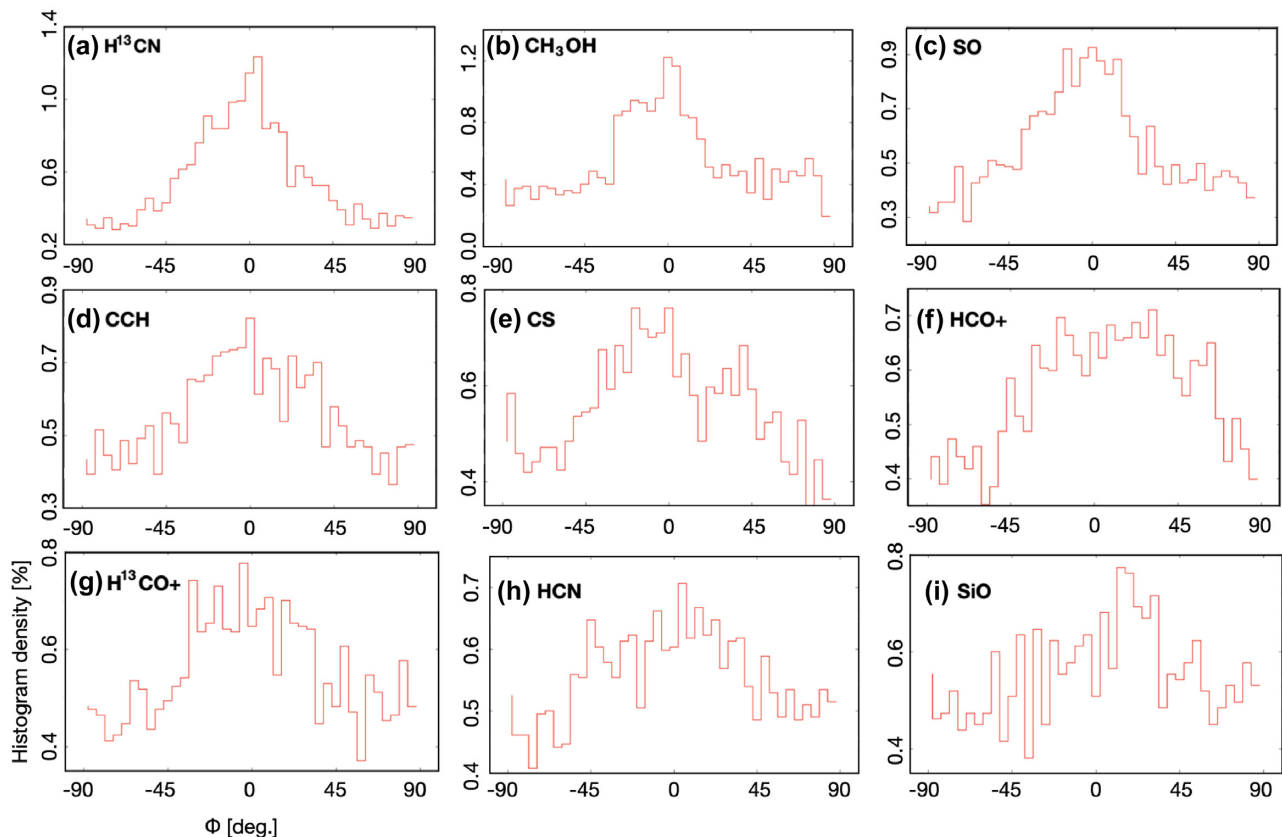


Figure 18. Histogram of relative orientation angles between molecular line emission and 3-mm continuum emission.

Table 7. Integrated intensities of molecular lines in ACA and 12-m-array observations.

Molecule	Size (arcsec ²)	ACA ^a		12-m ^b	Ratio
		Peak (Jy beam ⁻¹ km s ⁻¹)	Total (Jy km s ⁻¹)	Total (Jy km s ⁻¹)	
H ¹³ CN	17.6 × 11.4 arcsec ² (149°)	15.3	32.3	13.5	0.42
H ¹³ CO ⁺	24.0 × 12.5 arcsec ² (127°)	15.0	38.1	11.2	0.29
CCH	26.2 × 13.5 arcsec ² (142°)	13.0	38.7	8.7	0.23
SiO	18.1 × 11.4 arcsec ² (93°)	10.3	20.7	4.6	0.22
HCN	34.3 × 22.0 arcsec ² (131°)	12.1	46.4	8.5	0.18
HCO ⁺	31.4 × 15.7 arcsec ² (137°)	23.6	89.3	15.3	0.17
CH ₃ OH	13.7 × 7.0 arcsec ² (122°)	10.6	17.2	10.1	0.59
CS	23.5 × 13.7 arcsec ² (135°)	53.9	166.3	38.1	0.23
SO	17.2 × 10.9 arcsec ² (119°)	28.8	62.2	19.4	0.31
HC ₃ N	15.4 × 8.9 arcsec ² (140°)	34.5	70.2	35.9	0.51

^aThe parameters from ACA data were from 2D Gaussian fits.

^bThe total integrated intensities of molecular lines in 12-m-array data are measured within the massive filament region bounded by the 1 per cent of peak flux density contour ($\sim 3.5\sigma$ level) of the 3-mm continuum emission.

Orion distance). The Orion B project aims to obtain an accurate 3D description of the molecular structure in a GMC and to reveal the detailed anatomy of a molecular emission that is usually hidden behind these galaxy-averaged spectra in nearby galaxy studies. The ATOMS survey has comparable or better spatial resolution (< 0.05 pc) than the Orion B project for the 98 targeted Galactic clumps within 5 kpc. The ATOMS survey aims to reveal the detailed spatial distributions of molecular line emission inside a large sample of Galactic clumps and shares similar science goals as the Orion B project. The comparative studies with the Orion B data and the ATOMS data will shed light on the spatial distributions of molecular

emission across a widely different environment from a nearby GMC to distant massive star-forming regions.

The ‘EMIR Multiline Probe of the ISM Regulating Galaxy Evolution’ (EMPIRE; PI: Frank Bigiel) survey is a multiline mapping survey at the IRAM 30-m telescope that is targeting high critical density molecular lines ($J = 1-0$ of HCN, HCO⁺, and HNC) and CO isotopologues across the discs of nine nearby, star-forming, disc galaxies (Jiménez-Donaire et al. 2019). With an angular resolution of 30 arcsec at 90 GHz (or 1–2 kpc), The EMPIRE survey aims to constrain dense gas fraction and SFE across galaxy discs and explore how they depend on local conditions (molecular fraction,

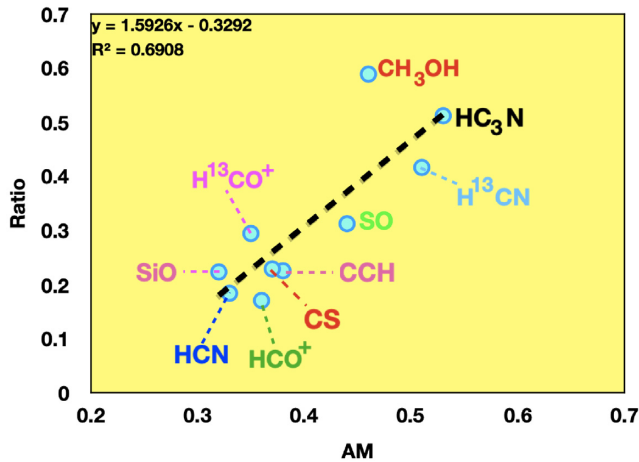


Figure 19. The ratio of $S_v^{1.2m}$ to S_v^{ACA} is plotted as a function of the alignment measurement (AM) in HOG analysis for 3-mm continuum and molecular line emission.

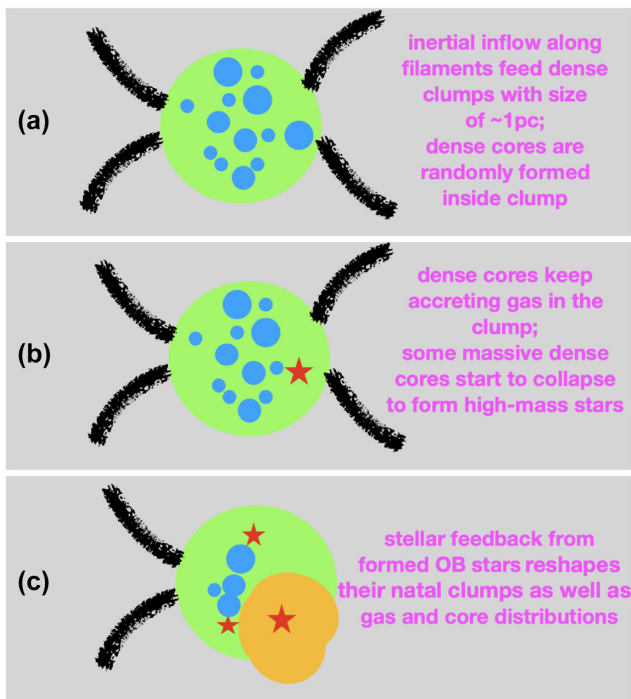


Figure 20. Sketch of the scenario to explain the sequential high-mass star formation in G9.62+0.19. Green filled circle is the massive clump with a typical size of 1 pc. The black lines represent converging flows connected to the clump. Blue filled circles are dense cores with a typical size of 0.1 pc. Red stars represent formed OB stars. The orange area in panel (c) shows an expanding H II region.

hydrostatic pressure, radiation field, stellar potential, etc.). The ATOMS survey also aims to investigate the star formation scaling relations with the same high critical density gas tracers, e.g. $J = 1-0$ of HCN, HCO⁺, and their isotopologue lines, and also to study how SFE changes across the inner Galaxy. The joint analysis of the ATOMS data and EMPIRE data will link ‘dense gas’ from the Milky Way to external galaxies.

The ‘ALMA_IMF: ALMA transforms our view of the origin of stellar masses’ (PI: Frédérique Motte) observed 15 most massive

clouds within 6 kpc at 3- and 1.3-mm at the ~ 2000 au spatial resolution. The ALMA_IMF project aims to constrain the proto-cluster core mass function (CMF) in the range $0.5-200 M_{\odot}$ and to investigate which variables (such as inflows, outflows, or forming filaments) might be correlated with CMF evolution in protoclusters. In contrast, the desired 3-mm continuum rms level in the ATOMS survey is of $\sim 65 \mu\text{Jy}$, corresponding to a mass sensitivity $\sim 2 M_{\odot}$ at a distance of 1 kpc and $\sim 50 M_{\odot}$ at a distance of 5 kpc (Kauffmann, Bertoldi & Bourke 2008). The mass sensitivity is derived with a median dust temperature of 30 K and a dust opacity per unit gas mass of $0.00189 \text{ cm}^2 \text{ g}^{-1}$ at 3 mm that is extrapolated from the dust opacity of $0.01 \text{ cm}^2 \text{ g}^{-1}$ at 230 GHz assuming a dust opacity index (β) of 2 (Ossenkopf & Henning 1994). Therefore, the ATOMS project will help constrain the high-mass end of the CMFs in protoclusters with a much larger sample but a shallower mass sensitivity than the ALMA_IMF project.

Another ALMA survey project, ‘ALMAGAL: ALMA Evolutionary study of High Mass Protocluster Formation in the Galaxy’ (PI: Sergio Molinari), will observe more than 1000 dense clumps with $M > 500 M_{\odot}$ and $d < 7.5$ kpc with similar linear resolution (~ 1000 au) and a mass sensitivity of $0.3 M_{\odot}$ at 1.3 mm. The ALMAGAL project will systematically investigate what the physical characteristics of core fragments in dense clumps are as a function of evolution and to what extent fragmentation is driven by dynamics in clumps or mass transport in filaments. The angular resolution and mass sensitivity of the ALMAGAL project are much better than the ATOMS project. However, the ATOMS survey benefits from the (~ 3 times) larger FOV at 3 mm than that of the ALMAGAL project at 1.3 mm, indicating that the ATOMS survey are more suitable to study the overall structures and kinematics in protoclusters. The comparative studies with the ALMAGAL data and the ATOMS data will help deepen the understandings of hierarchical fragmentation and differential star formation in high-mass protoclusters.

5 CONCLUSIONS

We introduce in this paper the observations, data reduction, and example science case, G9.62+0.19 (I18032–2032), of the ALMA survey programme ATOMS. The ATOMS project, standing for ALMA Three-millimeter Observations of Massive Star-forming regions, has observed 146 active star-forming regions at band 3 in both continuum emission and molecule lines. More than 90 per cent of the ATOMS targeted sources are promising high-mass star-forming regions. The ATOMS survey aims to systematically investigate the spatial distribution of various dense gas tracers, the roles of stellar feedback, and filaments in star formation.

(1) The 3-mm continuum data of the ATOMS survey will be used to detect massive filaments and dense cores. In G9.62+0.19, the 3-mm continuum emission reveals an expanding H II region ‘B’ to the west and a massive fragmented filament to the east. The 3-mm continuum emission of the expanding H II region ‘B’, compact H II region ‘MM1/C’, and the UC H II region ‘M11/D’ seem to be dominated by free-free emission.

(2) The ATOMS survey covers dozens of molecular line transitions, including shocked gas tracers (SiO, SO), a PDR tracer (CCH), hot core tracers (e.g. HC₃N and CH₃OH), and some lines commonly assumed to trace dense gas (e.g. HCN, HCO⁺, and CS). It also includes a tracer of ionized gas (H_{40 α} recombination line). We will investigate the spatial distributions of various gas tracers within a large sample of massive clumps. In G9.62+0.19, the similarities and differences in images of 10 molecular lines in

Table 2 are investigated with the PCA and the HOGs analysis. We found that the 10 lines can be classified into three groups. The first group includes CS, HCO⁺, HCN, CCH, and H¹³CO⁺, which mainly trace extended gas emission. SiO in the second group stands out from other molecules because it mainly traces shocked gas. The third group including SO, CH₃OH, H¹³CN, and HC₃N traces well dense gas in the massive filaments. Molecules in the same group show strongest correlations in their spatial distribution. SO, CH₃OH, H¹³CN, and HC₃N show morphology similar to that of the 3-mm continuum emission. The other molecular lines including the commonly used dense gas tracers, e.g. CS $J = 2 - 1$, $J = 1 - 0$ of HCO⁺ and HCN, can not reveal well dense structures (dense cores and filament) in G9.62+0.19 on the scale of ~ 0.1 pc.

(3) In the ATOMS survey, we will for the first time investigate statistically the origin of various velocity shocks using shock tracers like SiO. In G9.62+0.19, SiO shows widespread narrow emission, which is likely caused by slow shocks generated by large-scale colliding flows and HII regions.

(4) In the ATOMS survey, we will identify outflows driven by protostars. For G9.62+0.19, SiO, SO, CS, HCO⁺, and HCN trace well high-velocity outflow gas emission. The outflows, as traced by these molecular lines, show very similar morphology.

(5) The ATOMS survey covers a wide frequency range that includes dozens of molecular transitions that can be used to study chemical differentiation among dense cores. In G9.62+0.19, three dense cores (MM4/E, MM7/G, and MM8/F) show hot core chemistry.

(6) The ATOMS survey aims to statistically evaluate what fraction of gas in gravitationally bound clumps is actually participating in star formation or is concentrated in the smallest star formation units, i.e. dense cores. In G9.62+0.19, only less than 25 per cent of the ‘dense gas’ revealed by HCN, CS, and HCO⁺ is concentrated in the massive filament.

(7) The ATOMS survey aims to investigate how stellar feedback from formed OB (proto)stars in protoclusters affect their natal clumps and SFE. Stellar feedback from formed OB stars (H II region ‘B’) in G9.62+0.19 has reshaped their natal clump and changed the spatial distribution of gas and dense cores. Stellar feedback may be also the cause of the sequential high-mass star formation that is taking place in G9.62+0.19 complex.

(8) Joint analysis with the ATOMS survey data and other survey data, such as MALT90, Orion B, EMPIRE, ALMA-IMF, and ALMAGAL, will help deepen our understandings of ‘dense gas’ star formation scaling relations and massive protocluster formation.

ACKNOWLEDGEMENTS

Tie Liu is supported by the initial funding of scientific research for high-level talents at Shanghai Astronomical Observatory. This work was carried out in part at the Jet Propulsion Laboratory, which is operated for NASA by the California Institute of Technology. GG and LB acknowledges support from CONICYT project Basal AFB-170002. DL is supported by CAS International Partnership Program No. 114A11KYSB20160008. CWL is supported by the Basic Science Research Program through the National Research Foundation of Korea (NRF) funded by the Ministry of Education, Science and Technology (NRF-2019R1A2C1010851). This paper makes use of the following ALMA data: ADS/JAO.ALMA#2019.1.00685.S. ALMA is a partnership of ESO (representing its member states), NSF (USA), and NINS (Japan), together with NRC (Canada), MOST and ASIAA (Taiwan), and KASI (Republic of Korea),

in cooperation with the Republic of Chile. The Joint ALMA Observatory is operated by ESO, AUI/NRAO, and NAOJ.

REFERENCES

- Aladro R. et al., 2015, *A&A*, 579, A101
 Allen V., van der Tak F. F. S., Sánchez-Monge Á., Cesaroni R., Beltrán M. T., 2017, *A&A*, 603, 133
 André P., Arzoumanian D., Könyves V., Shimajiri Y., Palmeirim P., 2019, *A&A*, 629, L4
 André P., Di Francesco J., Ward-Thompson D., 2014, Beuther H., Klessen R. S., Dullemond C. P., Henning Th., eds, *Protostars and Planets VI*. Univ. of Arizona Press, Tucson, AZ, p. 914
 André P. et al., 2010, *A&A*, 518, 102
 Arzoumanian D. et al., 2011, *A&A*, 529, 6
 Arzoumanian D. et al., 2019, *A&A*, 621, 42
 Barnes P. J., Hernandez A. K., O’Dougherty S. N., 2016, *ApJ*, 831, 67
 Berry D. S., 2015, *A&C*, 10, 22
 Berry D. S., Reinhold K., Jenness T., Economou F., 2007, in Shaw R. A., Hill F., Bell D. J., eds, *ASP Conf. Ser. Vol. 376, ADASS XVI*. Astron. Soc. Pac., San Francisco, p. 425
 Beuther H., Semenov D., Henning T., Linz H., 2008, *ApJ*, 675, L33
 Bigiel F., Leroy A., Walter F., Brinks E., de Blok W. J. G., Madore B., Thornley M. D., 2008, *AJ*, 136, 2846
 Bonnell I. A., 2008, *ASP Conf. Ser. Vol. 390, Pathways Through an Eclectic Universe*. Astron. Soc. Pac., San Francisco, p. 26
 Bonnell I. A., Bate M. R., 2006, *MNRAS*, 370, 488
 Bonnell I. A., Bate M. R., Clarke C. J., Pringle J. E., 2002, *MNRAS*, 323, 785
 Bressert E., Ginsburg A., Bally J., Battersby C., Longmore S., Testi L., 2012, *ApJ*, 758, L28
 Bronfman L., Nyman L.-A., May J., 1996, *A&AS*, 115, 81
 Chen H., Gao Y., Braine J., Gu Q. et al., 2015, *ApJ*, 810, 140
 Chen H. et al., 2019, *ApJ*, 875, 24
 Chen X., Bourke T. L., Launhardt R., Henning T., 2008, *ApJ*, 686, 107
 Clarke S. D., Whitworth A. P., 2015, *MNRAS*, 449, 1819
 Condon J. J., Ransom S. M., 2016, *Essential Radio Astronomy*. Princeton Univ. Press, Princeton, NJ
 Contreras Y. et al., 2018, *ApJ*, 861, 14
 Cosentino G. et al., 2018, *MNRAS*, 474, 3760
 Cosentino G. et al., 2019, *ApJ*, 881, 42
 Cuadrado S., Goicoechea J. R., Pilleri P., Cernicharo J., Fuente A., Joblin C. et al., 2015, *A&A*, 575, A82
 Dall’Olio D. et al., 2019, *A&A*, 626, 36
 Dobbs C. L., Burkert A., Pringle J. E., 2011, *MNRAS*, 413, 2935
 Eden D. J. et al., 2017, *MNRAS*, 469, 2163
 Eden D. J. et al., 2019, *MNRAS*, 485, 2895
 Elmegreen B. G., Lada C. J., 1977, *ApJ*, 214, 725
 Enoch M. L., Glenn J., Evans N. J. II., Sargent A. I., Young K. E., Huard T. L., 2007, *ApJ*, 666, 982
 Esplugues G. B., Tercero B., Cernicharo J., 2013, *A&A*, 556, 143
 Evans N. J. II, 1999, *ARA&A*, 37, 311
 Evans N. J. II, Heiderman A., Vutisalchavakul N., 2014, *ApJ*, 782, 114
 Evans N. J. II, Kim K.-T., Wu J.-W., 2020, *ApJ*, 894, 103
 Faúndez S., Bronfman L., Garay G., Chini R., Nyman L. -Å., May J., 2004, *A&A*, 426, 97
 Gao Y., Solomon P. M., 2004, *ApJ*, 606, 271
 Garay G., Rodriguez L. F., Moran J. M., Churchwell E., 1993, *ApJ*, 418, 368
 Ginsburg A. et al., 2013, *ApJS*, 208, 14
 Goicoechea J. R., Pety J., Cuadrado S., 2016, *Nature*, 537, 207
 González Lobos V., Stutz A. M., 2019, *MNRAS*, 489, 4771
 Greve T. R. et al., 2014, *ApJ*, 794, 142
 Hacar A., Kainulainen J., Tafalla M., Beuther H., Alves J., 2016, *A&A*, 587, 97
 Hacar A., Tafalla M., Forbrich J., Alves J., Meingast S., Grossschedl J., Teixeira P. S., 2018, *A&A*, 610, 77

- Hacar A., Tafalla M., Kauffmann J., Kovács A., 2013, *A&A*, 554, 55
- Heiderman A., Evans N. J. II, Allen L. E., Huard T., Heyer M., 2010, *ApJ*, 723, 1019
- Hofner P., Kurtz S., Churchwell E., Walmsley C. M., Cesaroni R., 1994, *ApJ*, 429, L85
- Hofner P., Kurtz S., Churchwell E., Walmsley C. M., Cesaroni R., 1996, *ApJ*, 460, 359
- Hofner P., Wiesemeyer H., Henning T., 2001, *ApJ*, 549, 425
- Hoq S. et al., 2013, *ApJ*, 777, 157
- Jackson J. M., Rathborne J. M., Foster J. B., 2013, *PASA*, 30, 57
- Jiménez-Donaire M. J., et al., 2019, *ApJ*, 880, 127
- Jiménez-Serra I., Caselli P., Tan J. C., Hernandez A. K., Fontani F., Butler M. J., van Loo S., 2010, *MNRAS*, 406, 187
- Jones P. A., Burton M. G., Cunningham M. R., Tothill N. F. H., Walsh A. J., 2013, *MNRAS*, 433, 221
- Jones P. A. et al., 2012, *MNRAS*, 419, 2961
- Juvela M. et al., 2012, *A&A*, 541, 12
- Kainulainen J., Stutz A. M., Stanke T., Abreu-Vicente J., Beuther H., Henning T., Johnston K. G., Megeath S.T., 2017, *A&A*, 600, A141
- Kauffmann J., Bertoldi F., Bourke T. L., 2008, *A&A*, 487, 993
- Kauffmann J., Goldsmith P. F., Melnick G., Tolls V., Guzman A., Menten K. M., 2017, *A&A*, 605, L5
- Kauffmann J., Pillai T., 2010, *ApJ*, 723, L7
- Kennicutt R. C., Evans N. J., 2012, *ARA&A*, 50, 531
- Kennicutt R. C., Jr, 1998a, *ApJ*, 498, 541
- Kennicutt R. C., Jr, 1998b, *ARA&A*, 36, 189
- Kirk H., Myers P. C., Bourke T. L., Gutermuth R. A., Hedden A., Wilson G. W., 2013, *ApJ*, 766, 115
- Krumholz M. R., Bate M. R., Arce H. G. et al., 2014, in Beuther H, Klessen R. S., Dullemond C. P., Henning T., eds, *Protostars and Planets VI*. Univ. Arizona Press, Tucson, AZ, p. 914
- Krumholz M. R., Klein R. I., McKee C. F., 2011, *ApJ*, 740, 74
- Krumholz M. R., McKee C. F., 2008, *Nature*, 451, 1082
- Könyves V. et al., 2015, *A&A*, 584, 91
- Lada C. J., Forbrich J., Lombardi M., Alves J. F., 2012, *ApJ*, 745, 190
- Lada C. J., Lombardi M., Alves J. F., 2010, *ApJ*, 724, 687
- Lazarian A., Hoang T., 2007, *MNRAS*, 378, 910
- Le Page V., Snow T. P., Bierbaum V. M., 2003, *ApJ*, 584, 316
- Liu D., Gao Y., Isaak K., Daddi E., Yang C., Lu N., van der Werf P., 2015a, *ApJ*, 810, 14
- Liu H. B., Chen H.-R. V., Román-Zúñiga C. G., 2019, *ApJ*, 871, 185
- Liu H. B., Galván-Madrid R., Jiménez-Serra I., Román-Zúñiga C., Zhang Q., Li Z., Chen H.-R., 2015b, *ApJ*, 804, 37
- Liu H. B., Jiménez-Serra I., Ho P. T. P., Chen H.-R., Zhang Q., Li Z.-Y., 2012, *ApJ*, 756, 10
- Liu T., Wu Y., Liu S.-Y., Qin S.-L., Su Y.-N., Chen H.-R., Ren Z., 2011, *ApJ*, 730, 102
- Liu T. et al., 2016, *ApJ*, 829, 59
- Liu T. et al., 2017, *ApJ*, 849, 25
- Liu T. et al., 2018a, *ApJS*, 234, 28
- Liu T. et al., 2018b, *ApJ*, 859, 151
- Liu T. et al., 2018c, *ApJ*, 869, L5
- Liu T. et al., 2020, *MNRAS*, 496, 2821
- Lo N. et al., 2009, *MNRAS*, 395, 1021
- Louvet F. et al., 2016, *A&A*, 595, 122
- Lu X. et al., 2018, *ApJ*, 855, 9
- McMullin J. P., Waters B., Schiebel D., Young W., Golap K., 2007, in Shaw R. A., Hill F., Bell D. J., eds, *ASP Conf. Ser. Vol. 376, ADASS XVI*. Astron. Soc. Pac., San Francisco, p.127
- Molinari S., Pezzuto S., Cesaroni R., Brand J., Faustini F., Testi L., 2008, *A&A*, 481, 345
- Molinari S. et al., 2010, *A&A*, 518, 100
- Montillaud J., Joblin C., Toubanc D., 2013, *A&A*, 552, A15
- Moscadelli L. et al., 2018, *A&A*, 616, 66
- Myers A. T., McKee C. F., Cunningham A. J., Klein R. I., Krumholz M.R., 2013, *ApJ*, 766, 97
- Möller T., Endres C., Schilke P., 2017, *A&A*, 598, A7
- Nagy Z., Spezzano S., Caselli P., Vasyunin A., Tafalla M., Bizzocchi L., Prudeniano D., Redaelli E., 2019, *A&A*, 630, 136
- Nguyen-Luong Q. et al., 2020, *ApJ*, 891, 66
- Nguyen-Lu'o'ng Q. et al., 2013, *ApJ*, 775, 88
- Offner S. S. R., Klein R. I., McKee C. F., 2009, *ApJ*, 703, 131
- Ossenkopf V., Henning T., 1994, *A&A*, 291, 943
- Padoan P., Pan L., Juvela M., Haugbølle T., Nordlund Å., 2019, *ApJ*, preprint ([arXiv:1911.04465](https://arxiv.org/abs/1911.04465))
- Papadopoulos P. P., 2007, *ApJ*, 656, 792
- Peng Y., Rivilla V. M., Zhang L., Ge J. X., Zhou B., 2019, *ApJ*, 871, 251
- Peng Y. et al., 2017, *ApJ*, 837, 49
- Peretto N. et al., 2013, *A&A*, 555, 112
- Pety J., Teyssier D., Fossé D., Gerin M., Roueff E., Abergel A., Habart E., Cernicharo J., 2005, *A&A*, 435, 885
- Pety J. et al., 2017, *A&A*, 599, A98
- Pillepich A. et al., 2018, *MNRAS*, 473, 4077
- Pols S., Schwörer A., Schilke P., Schmiedeke A., Sánchez-Monge Á., Möller Th., 2018, *A&A*, 614, 123
- Pon A., Johnstone D., Heitsch F., 2011, *ApJ*, 740, 88
- Pon A., Toalá J. A., Johnstone D., Vázquez-Semadeni E., Heitsch F., Gómez G. C., 2012, *ApJ*, 756, 145
- Pratap P., Dickens J. E., Snell R. L., Miralles M. P., Bergin E. A., Irvine W. M., Schloerb F. P., 1997, *ApJ*, 486, 862
- Qin S.-L., Schilke P., Wu J., Wu Y., Liu T., Liu Y., Sánchez-Monge A., 2015, *ApJ*, 803, 39
- Quiroza C., Rood R. T., Bania T. M., Balsa D.S., Maciel W. J., 2006, *ApJ*, 653, 1226
- Sanhueza P., Jackson J. M., Foster J. B., Garay G., Silva A., Finn S. C., 2012, *ApJ*, 756, 60
- Sanhueza P. et al., 2019, *ApJ*, 886, 102
- Sanna A., Reid M. J., Moscadelli L., Dame T. M., Menten K. M., Brunthaler A., Zheng X. W., Xu Y., 2009, *ApJ*, 706, 464
- Saraceno P., Andre P., Ceccarelli C., Griffin M., Molinari S., 1996, *A&A*, 309, 827
- Schisano E. et al., 2020, *MNRAS*, 492, 5420
- Schmidt M., 1959, *ApJ*, 129, 243
- Shimajiri Y. et al., 2017, *A&A*, 604, A74
- Shirley Y. L., 2015, *PASP*, 127, 299
- Silk J., 1997, *ApJ*, 481, 703
- Soler J. D. et al., 2019, *A&A*, 622A, 166
- Solomon P. M., Downes D., Radford S. J. E., Barrett J. W., 1997, *ApJ*, 478, 144
- Spezzano S., Caselli P., Bizzocchi L., 2017, *A&A*, 606, 82S
- Stephens I. W., Jackson J. M., Whitaker J. S., 2016, *ApJ*, 824, 29
- Stutz A. M., 2018, *MNRAS*, 473, 4890
- Stutz A. M., Gould A., 2016, *A&A*, 590, A2
- Tacconi L. J., Genzel R., Sternberg A., 2020, *ARA&A*, preprint ([arXiv:2003.06245](https://arxiv.org/abs/2003.06245))
- Tan Q. et al., 2018, *ApJ*, 860, 165
- Testi L., Hofner P., Kurtz S., Rupen M., 2000, *A&A*, 359, L5
- Thompson M. A., Urquhart J. S., Moore T. J. T., Morgan L. K., 2012, *MNRAS*, 421, 408
- Tiwari M., Menten K. M., Wyrowski F., Pérez-Beaupuits J. P., Lee M. -Y., Kim W. -J., 2019, *A&A*, 626, 28
- Tobin J. J., Bourke T. L., Mader S., 2019, *ApJ*, 870, 81
- Urquhart J. S., König C., Giannetti A., 2018, *MNRAS*, 473, 1059
- Urquhart J. S. et al., 2014, *MNRAS*, 443, 1555
- Vogelsberger M. et al., 2014, *Nature*, 509, 177
- Vutisalchavakul N., Evans N. J. II, Heyer M., 2016, *ApJ*, 831, 73
- Wall J. E., Mac Low M., McMillan S. L. W., Klessen R. S., Portegies Z. S., Pellegrino A., 2020, *AAS*, preprint ([arXiv:2003.09011](https://arxiv.org/abs/2003.09011))
- Wang K., Testi L., Burkert A., Walmsley C. M., Beuther H., Henning T., 2016, *ApJS*, 226, 9
- Wang K., Zhang Q., Wu Y., 2011, *ApJ*, 735, 64
- Wang K., Zhang Q., Wu Y., 2012, *ApJ*, 745, 30
- Wang K. et al., 2014, *MNRAS*, 439, 3275
- Whitworth A. P., Bhattal A. S., Chapman S. J., Disney M. J., Turner J. A., 1994a, *A&A*, 290, 421

Whitworth A. P., Bhattal A. S., Chapman S. J., Disney M. J., Turner J. A., 1994b, *MNRAS*, 268, 291
 Wu J., Evans N. J. II, Gao Y., Soloman P. M., Shirley Y. L., Vanden Bout P. A., 2005, *ApJ*, 635, L173
 Wu J., Evans N. J. II, Shirley Y. L., Knez C., 2010, *ApJS*, 188, 313
 Yuan J. et al., 2017, *ApJS*, 231, 11
 Zhang Q., Wang K., 2011, *ApJ*, 733, 26

Zhang Q., Wang K., Lu X., 2015, *ApJ*, 804, 141
 Zhang Z.-Y., Gao Y., Henkel C., Zhao Y., Wang J., Menten K. M., Güsten R., 2014, *ApJ*, 784, L31
 Zhu F.-Y., Zhu Q.-F., Wang J.-Z., Zhang J.-S., 2019, *ApJ*, 881, 14

APPENDIX A

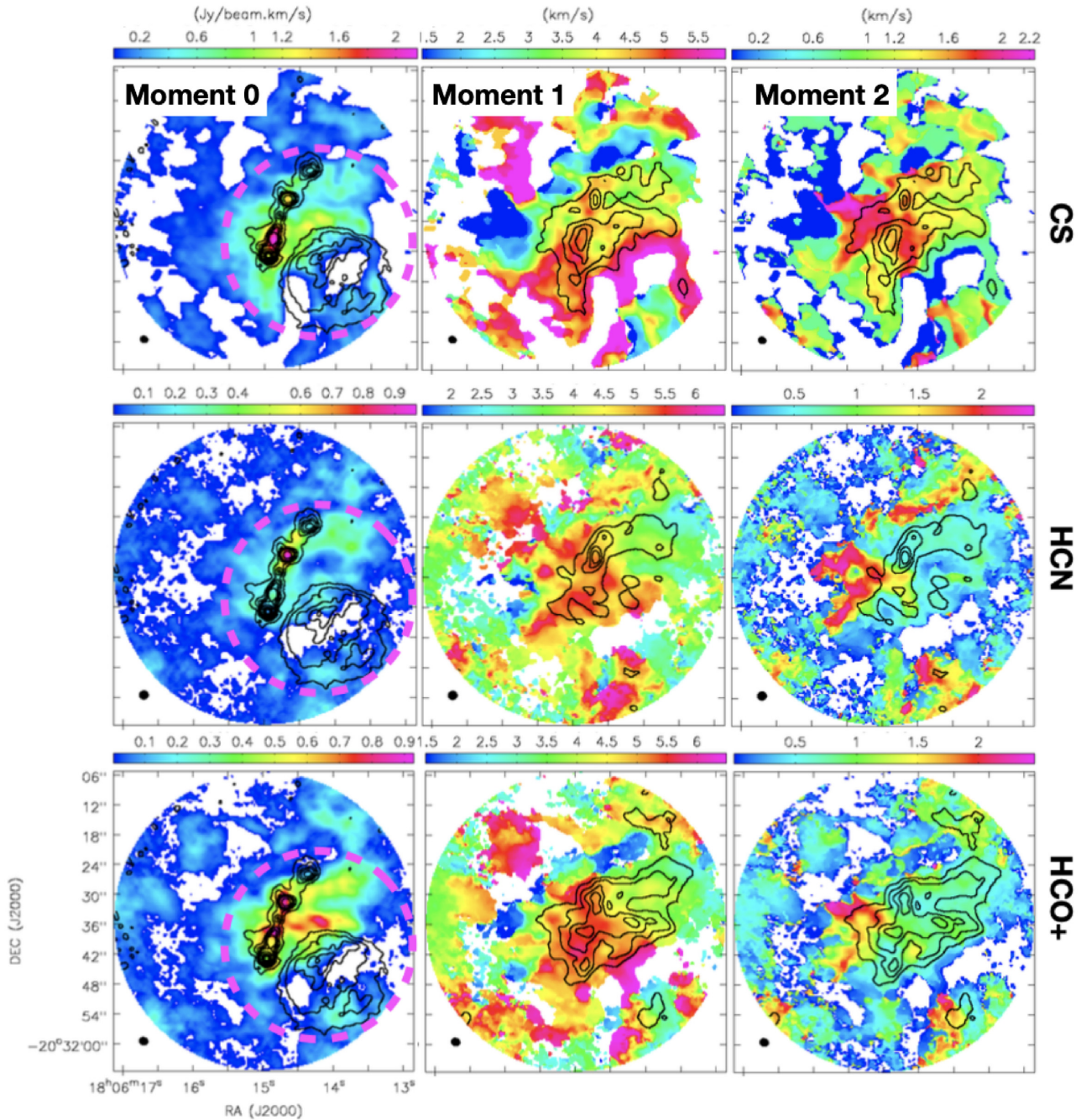


Figure A1. The left-hand, middle, and right-hand columns present the integrated intensity (Moment 0) maps, intensity-weighted velocity maps (Moment 1), and intensity-weighted velocity dispersion (Moment 2) maps of G9.62+0.19 for the gas tracers indicated on the right-hand side of each row. The names of tracers are labelled to the right-hand side. The contours on Moment 0 maps show the 3 mm continuum emission. The contour levels are $[0.01, 0.03, 0.05, 0.07, 0.1, 0.2, 0.4, 0.6, 0.8] \times 74.1 \text{ mJy beam}^{-1}$. The contours on Moment 1 and Moment 2 maps show the corresponding integrated intensity maps of various gas tracers. The contours are $[0.2, 0.4, 0.6, 0.8] \times F_{\text{peak}}$. The peak integrated intensities (F_{peak}) for CS, HCN, HCO⁺ are 2.16, 0.97, and 0.93 $\text{Jy beam}^{-1} \text{ km s}^{-1}$, respectively. The magenta dashed circle on Moment 0 map shows the clump boundary traced by H¹³CN.

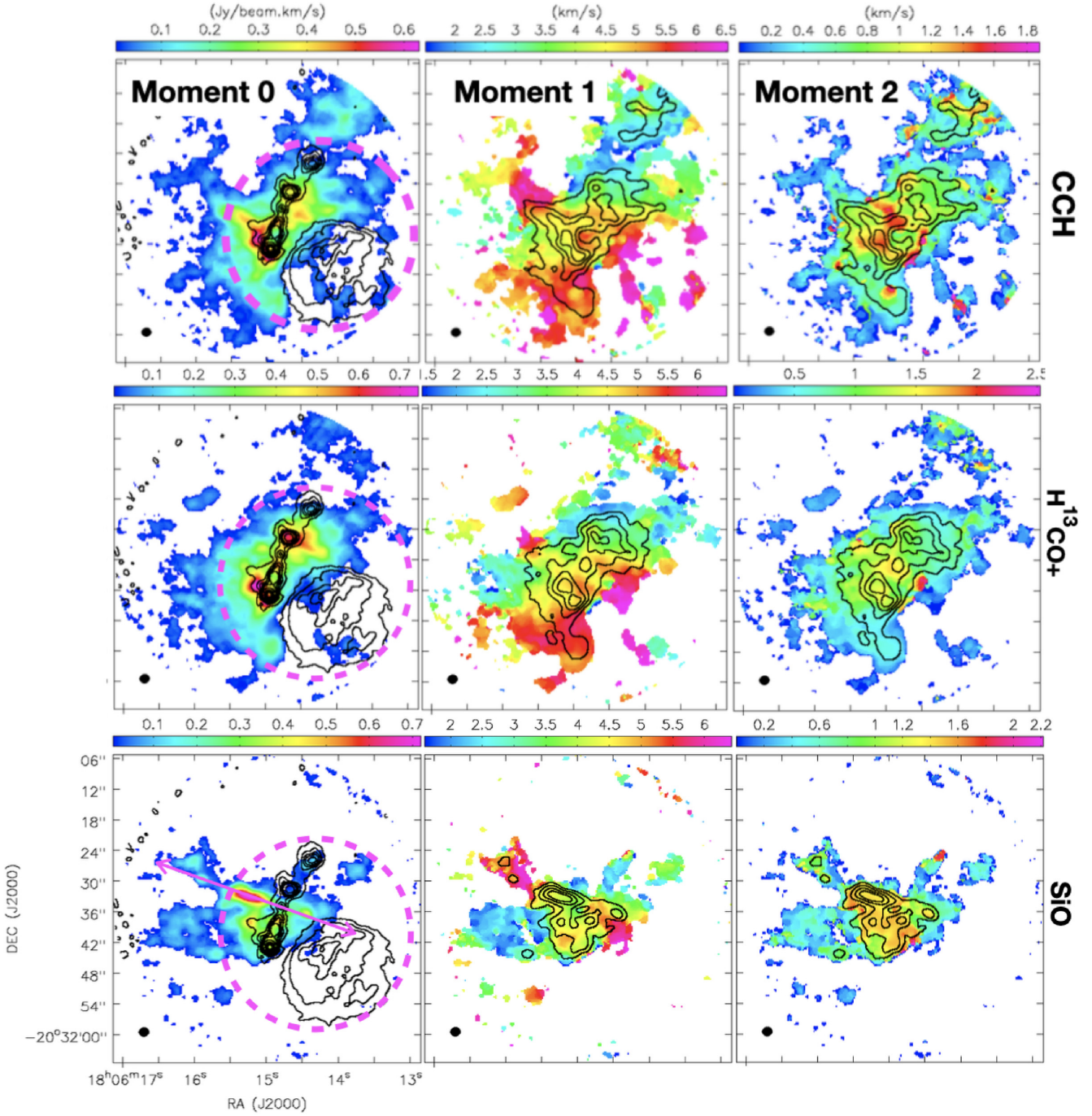


Figure A2. The images and contours are same as in Fig. A1. The peak integrated intensities (F_{peak}) for CCH, H¹³CO⁺, and SiO are 0.63, 0.75, and 0.72 Jy beam⁻¹ km s⁻¹, respectively. The magenta dashed circle on the Moment 0 maps show the clump boundary traced by H¹³CN. The magenta arrow represents the direction of the bipolar outflow driven by MM6.

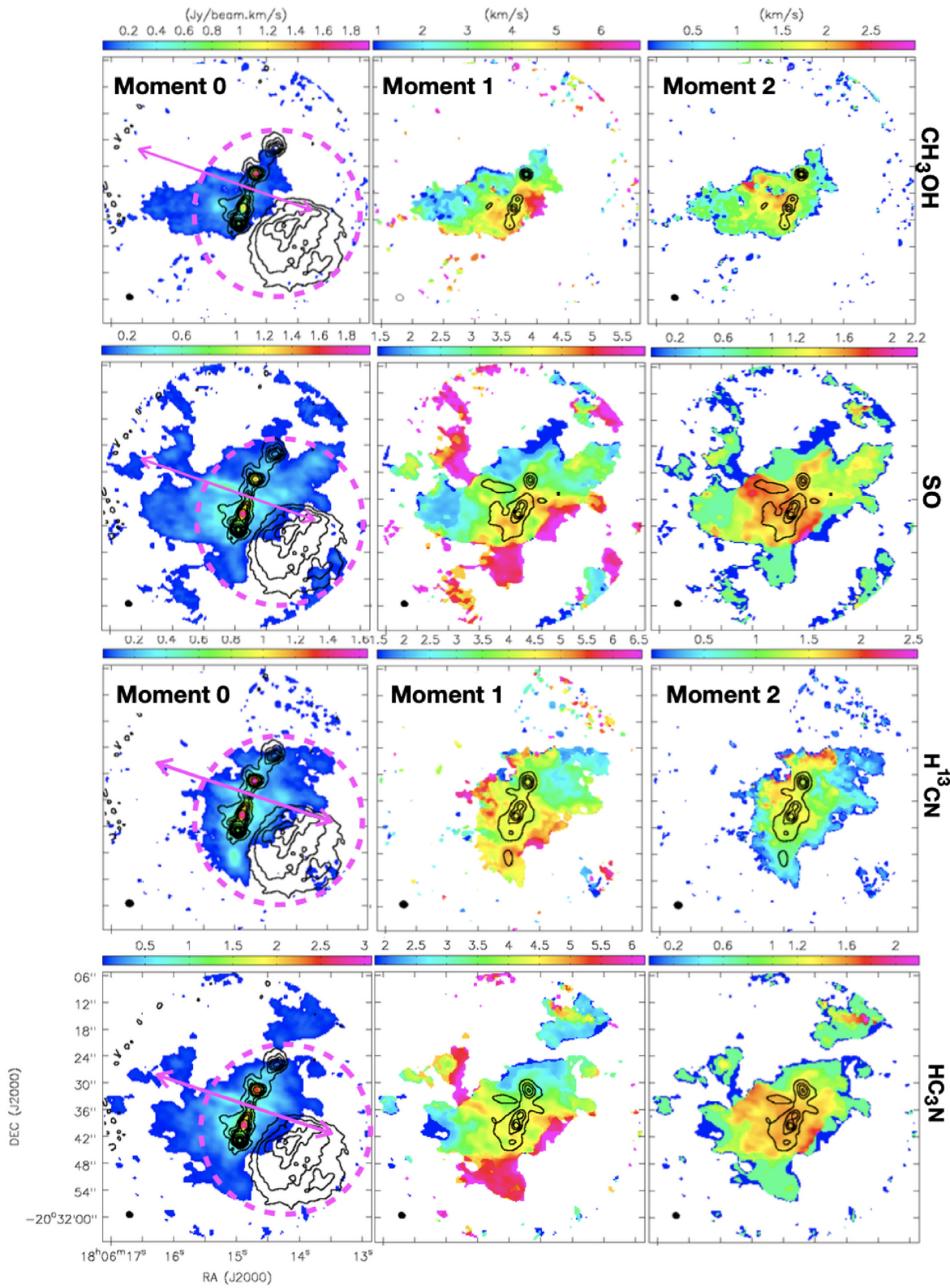


Figure A3. The images and contours are same as in Fig. A1. The peak integrated intensities (F_{peak}) for CH₃OH, SO, H¹³CN, and HC₃N are 1.94, 1.98, 1.65, and 3.09 Jy beam⁻¹ km s⁻¹, respectively. The magenta dashed circle on the Moment 0 maps show the clump boundary traced by H¹³CN. The magenta arrow represents the direction of the bipolar outflow driven by MM6.

Table A1. Basic parameters of the targets in the ATOMS survey.

ID	IRAS	RA	DEC	V_{lsr} (km s^{-1})	Distance (kpc)	R_{GC} (kpc)	Radius (pc)	T_{dust} (K)	$\log(L_{\text{bol}})$ (L_{\odot})	$\log(M_{\text{clump}})$ (M_{\odot})	References ^d
1	I08076–3556	08:09:32.39	–36:05:13.2	5.9	0.4	8.5	0.07	18.0	1.2	0.7	1
2	I08303–4303	08:32:08.34	–43:13:54.0	14.3	2.3	9.0	0.32	30.0	3.8	2.4	1
3	I08448–4343	08:46:32.90	–43:54:35.9	3.7	0.7	8.4	0.15	25.0	3.0	1.6	1
4	I08470–4243	08:48:47.07	–42:54:31.0	12	2.1	8.8	0.32	33.0	4.0	2.4	1
5	I09002–4732	09:01:54.24	–47:44:00.8	3.1	1.2	8.4	0.24	39.0	4.6	2.4	1
6	I09018–4816	09:03:32.84	–48:28:10.0	10.3	2.6	8.8	0.44	31.0	4.7	3.0	1
7	I09094–4803	09:11:07.29	–48:15:48.7	74.6	9.6	12.7	1.40	23.0	4.6	3.1	1
8	I10365–5803	10:38:32.46	–58:19:05.9	–19	2.4	8.0	0.44	30.0	4.3	2.7	1
9	I11298–6155	11:32:05.70	–62:12:24.3	32.9	10	10.1	1.36	32.0	5.2	3.4	1
10	I11332–6258	11:35:31.81	–63:14:44.6	–15.4	1.9	7.7	0.28	30.0	3.7	2.1	1
11	I11590–6452	12:01:34.54	–65:08:52.9	–4.3	0.4	8.2	0.06	22.0	1.7	1.1	1
12	I12320–6122	12:34:53.38	–61:39:46.9	–42.5	3.43	7.2	1.00	44.6	5.6	3.0	2
13	I12326–6245	12:35:34.81	–63:02:32.1	–39.6	4.61	7.2	0.83	34.2	5.4	3.5	2
14	I12383–6128	12:41:17.32	–61:44:38.6	–39.1	3.27	7.2	0.63	19.8	3.8	3.1	2
15	I12572–6316	13:00:24.43	–63:32:30.4	30.9	11.57	9.8	1.63	21.5	4.6	3.9	2
16	I13079–6218	13:11:14.16	–62:34:42.1	–42.6	3.8	6.9	1.09	28.2	5.1	3.5	2
17	I13080–6229	13:11:14.10	–62:45:01.9	–35.6	3.8	6.9	1.03	34.1	5.1	3.2	2
18	I13111–6228	13:14:26.43	–62:44:24.1	–38.8	3.8	6.9	0.96	30.0	4.8	3.1	2
19	I13134–6242	13:16:43.05	–62:58:30.1	–31.5	3.8	6.9	0.57	29.2	4.6	3.1	2
20	I13140–6226	13:17:15.70	–62:42:27.5	–33.9	3.8	6.9	0.50	22.6	3.8	2.9	2
21	I13291–6229	13:32:32.38	–62:45:23.5	–36.5	2.9	7.0	0.55	28.8	4.3	2.7	2
22	I13291–6249	13:32:31.23	–63:05:21.8	–34.7	7.61	7.1	1.73	27.2	5.2	3.7	2
23	I13295–6152	13:32:53.49	–62:07:49.3	–44.4	3.89	6.7	0.36	19.4	3.3	2.7	2
24	I13471–6120	13:50:42.10	–61:35:14.9	–56.7	5.46	6.4	1.01	35.1	5.3	3.4	2
25	I13484–6100	13:51:58.64	–61:15:43.3	–55	5.4	6.4	0.84	31.8	4.8	3.1	2
26	I14013–6105	14:04:54.56	–61:20:10.7	–48.1	4.12	6.4	0.80	31.4	5.0	3.2	2
27	I14050–6056	14:08:42.15	–61:10:43.0	–47.1	3.42	6.6	0.66	32.2	4.7	2.8	2
28	I14164–6028	14:20:08.23	–60:42:05.0	–46.5	3.19	6.6	0.17	28.7	3.7	2.2	2
29	I14206–6151	14:24:22.81	–62:05:22.7	–50	3.29	6.5	0.37	27.3	3.7	2.4	2
30	I14212–6131	14:25:01.08	–61:44:59.4	–50.5	3.44	6.5	0.57	21.8	4.0	3.0	2
31	I14382–6017	14:42:02.76	–60:30:35.1	–60.7	7.69	6.0	1.68	28.0	5.2	3.6	2
32	I14453–5912	14:49:07.77	–59:24:49.7	–40.2	2.82	6.6	0.79	24.1	4.2	2.9	2
33	I14498–5856	14:53:42.81	–59:08:56.5	–49.3	3.16	6.4	0.74	26.7	4.4	3.0	2
34	I15122–5801	15:16:06.77	–58:11:40.5	–60.9	9.26	5.9	2.65	27.7	5.0	3.9	2
35	I15254–5621	15:29:19.48	–56:31:23.2	–67.3	4	5.7	0.89	33.5	5.1	3.1	2
36	I15290–5546	15:32:53.16	–55:56:06.8	–87.5	6.76	4.9	1.80	33.5	5.7	3.8	2
37	I15384–5348	15:42:16.57	–53:58:31.3	–41	1.82	6.9	0.54	33.9	4.6	2.5	2
38	I15394–5358	15:43:16.48	–54:07:16.9	–41.6	1.82	6.9	0.46	20.7	3.7	2.9	2
39	I15408–5356	15:44:43.00	–54:05:44.9	–39.7	1.82	6.9	0.61	34.0	4.9	2.9	2
40	I15411–5352	15:44:59.59	–54:02:21.4	–41.5	1.82	6.9	0.57	30.5	4.5	2.7	2
41	I15437–5343	15:47:33.11	–53:52:43.9	–83	4.98	5.0	0.77	29.6	4.6	3.0	2
42	I15439–5449	15:47:49.82	–54:58:32.1	–54.6	3.29	5.9	0.69	26.8	4.4	3.0	2
43	I15502–5302	15:54:06.43	–53:11:38.4	–91.4	5.8	4.6	1.66	35.7	5.8	3.7	2
44	I15520–5234	15:55:48.84	–52:43:06.2	–41.3	2.65	6.2	0.67	32.2	5.1	3.2	2
45	I15522–5411	15:56:07.74	–54:19:57.8	–46.7	2.73	6.2	0.64	23.3	3.8	2.9	2
46	I15557–5215	15:59:40.76	–52:23:27.7	–67.6	4.03	5.3	0.82	20.7	3.9	3.2	2
47	I15567–5236	16:00:32.86	–52:44:45.1	–107.1	5.99	4.4	1.31	35.4	5.7	3.5	2
48	I15570–5227	16:00:55.56	–52:36:21.2	–101.5	5.99	4.4	1.66	28.7	4.8	3.4	2
49	I15584–5247	16:02:19.63	–52:55:22.4	–76.8	4.41	5.1	0.86	23.9	4.2	3.1	2
50	I15596–5301	16:03:32.29	–53:09:28.1	–72.1	10.11	5.2	1.81	28.5	5.5	3.9	2
51	I16026–5035	16:06:25.43	–50:43:07.2	–78.3	4.53	4.9	0.81	31.8	4.9	3.0	2
52	I16037–5223	16:07:38.10	–52:31:00.2	–80	9.84	4.9	2.15	31.4	5.6	3.8	2
53	I16060–5146	16:09:52.85	–51:54:54.7	–91.6	5.3	4.5	1.24	32.2	5.8	3.9	2
54	I16065–5158	16:10:20.30	–52:06:07.1	–63.3	3.98	5.2	1.41	30.8	5.4	3.7	2
55	I16071–5142	16:11:00.01	–51:50:21.6	–87	5.3	4.5	1.21	23.9	4.8	3.7	2
56	I16076–5134	16:11:27.12	–51:41:56.9	–87.7	5.3	4.5	1.57	30.1	5.3	3.6	2
57	I16119–5048	16:15:45.65	–50:55:53.5	–48.2	3.1	5.8	0.93	24.0	4.3	3.2	2
58	I16132–5039	16:17:01.52	–50:46:51.0	–47.5	3.1	5.8	1.04	32.5	4.6	2.9	2
59	I16158–5055	16:19:38.63	–51:03:20.0	–49.2	3.57	5.4	1.35	28.3	5.2	3.5	2
60	I16164–5046	16:20:10.91	–50:53:15.5	–57.3	3.57	5.4	1.37	31.4	5.5	3.7	2
61	I16172–5028	16:21:02.47	–50:35:10.3	–51.9	3.57	5.4	1.51	32.0	5.8	4.0	2
62	I16177–5018	16:21:31.49	–50:25:04.5	–50.2	3.57	5.4	1.25	34.0	5.5	3.6	2

Table A1 – continued

ID	IRAS	RA	DEC	V_{lsr} (km s^{-1})	Distance (kpc)	R_{GC} (kpc)	Radius (pc)	T_{dust} (K)	$\log(L_{\text{bol}})$ (L_{\odot})	$\log(M_{\text{clump}})$ (M_{\odot})	References ^a
63	I16272–4837	16:30:59.08	–48:43:53.3	–46.6	2.92	5.8	0.84	23.1	4.3	3.2	2
64	I16297–4757	16:33:29.45	–48:03:41.2	–79.6	5.03	4.2	2.00	27.1	4.9	3.4	2
65	I16304–4710	16:34:05.12	–47:16:32.6	–62.8	11.32	4.9	1.37	27.5	4.9	3.5	2
66	I16313–4729	16:34:54.98	–47:35:35.0	–73.7	4.71	4.4	2.06	31.0	6.7	4.7	1, 2
67	I16318–4724	16:35:34.11	–47:31:11.3	–119.8	7.68	3.3	1.45	29.5	5.2	3.7	2
68	I16330–4725	16:36:42.96	–47:31:29.7	–75.1	10.99	4.6	3.89	33.8	6.3	4.3	2
69	I16344–4658	16:38:09.38	–47:04:58.7	–49.5	12.09	5.4	2.70	25.5	5.4	4.1	2
70	I16348–4654	16:38:29.64	–47:00:41.1	–46.5	12.09	5.4	2.40	23.6	5.4	4.4	2
71	I16351–4722	16:38:50.98	–47:27:57.8	–41.4	3.02	5.7	0.69	30.4	4.9	3.2	2
72	I16362–4639	16:39:57.32	–46:45:06.3	–38.8	3.01	5.7	0.54	24.0	3.6	2.5	2
73	I16372–4545	16:40:54.57	–45:50:49.6	–57.3	4.16	4.7	0.73	26.0	4.2	2.9	2
74	I16385–4619	16:42:14.04	–46:25:25.9	–117	7.11	3.1	1.34	31.9	5.1	3.2	2
75	I16424–4531	16:46:06.61	–45:36:46.6	–34.2	2.63	6.0	0.54	24.6	3.9	2.7	2
76	I16445–4459	16:48:05.18	–45:05:08.6	–121.3	7.95	2.8	2.54	24.6	5.0	3.9	2
77	I16458–4512	16:49:30.41	–45:17:53.6	–50.4	3.56	5.1	1.42	21.4	4.5	3.6	2
78	I16484–4603	16:52:04.29	–46:08:30.1	–32	2.1	6.4	0.55	35.0	5.0	3.0	1, 2
79	I16487–4423	16:52:23.67	–44:27:52.3	–43.4	3.26	5.4	1.01	24.6	4.4	3.0	2
80	I16489–4431	16:52:33.50	–44:36:17.7	–41.3	3.26	5.4	0.71	21.8	3.8	2.9	2
81	I16506–4512	16:54:15.77	–45:17:31.8	–26.2	2.42	6.1	0.86	32.4	5.0	3.1	2
82	I16524–4300	16:56:03.06	–43:04:43.3	–40.8	3.43	5.2	1.06	23.4	4.4	3.4	2
83	I16547–4247	16:58:17.26	–42:52:04.5	–30.4	2.74	5.8	0.69	28.9	4.8	3.2	2
84	I16562–3959	16:59:41.42	–40:03:46.6	–12.6	2.38	6.1	0.72	42.3	5.7	3.2	2
85	I16571–4029	17:00:32.21	–40:34:12.7	–15	2.38	6.1	0.38	27.0	4.3	2.9	2
86	I17006–4215	17:04:12.99	–42:19:54.2	–23.2	2.21	6.3	0.50	27.7	4.4	2.8	2
87	I17008–4040	17:04:23.03	–40:44:24.9	–17	2.38	6.1	1.26	31.0	4.6	3.0	1, 2
88	I17016–4124	17:05:11.02	–41:29:07.8	–27.1	1.37	7.0	0.75	32.0	5.3	3.8	1, 2
89	I17136–3617	17:17:02.04	–36:20:52.5	–10.6	1.34	7.0	0.45	34.8	4.6	2.5	2
90	I17143–3700	17:17:45.65	–37:03:11.8	–31.1	12.67	4.7	2.95	31.0	5.6	3.8	2
91	I17158–3901	17:19:20.34	–39:03:53.3	–15.2	3.38	5.1	1.18	23.3	4.8	3.4	2
92	I17160–3707	17:19:26.81	–37:11:01.4	–69.5	10.53	2.7	1.69	28.5	6.0	4.1	2
93	I17175–3544	17:20:53.10	–35:47:03.0	–5.7	1.34	7.0	0.35	30.6	4.8	3.1	2
94	I17204–3636	17:23:50.32	–36:38:58.1	–18.2	3.32	5.1	0.60	25.8	4.2	2.9	2
95	I17220–3609	17:25:24.99	–36:12:45.1	–93.7	8.01	1.3	2.41	25.4	5.7	4.3	2
96	I17233–3606	17:26:42.73	–36:09:20.8	–2.7	1.34	7.0	0.37	29.9	4.6	3.0	2
97	I17244–3536	17:27:48.71	–35:39:10.8	–10.2	1.36	7.0	0.30	29.8	3.7	2.1	2
98	I17258–3637	17:29:16.99	–36:40:16.5	–11.9	2.59	5.8	0.92	45.5	5.9	3.3	2
99	I17269–3312	17:30:14.77	–33:14:57.5	–21	4.38	4.0	1.53	22.4	4.7	3.6	2
100	I17271–3439	17:30:26.21	–34:41:48.9	–18.2	3.1	5.3	1.34	35.0	5.6	4.0	1, 2
101	I17278–3541	17:31:14.07	–35:44:07.3	–0.4	1.33	7.0	0.31	25.1	3.8	2.5	2
102	I17439–2845	17:47:09.20	–28:46:13.9	18.7	8	0.3	1.78	30.0	5.7	3.8	1
103	I17441–2822	17:47:19.79	–28:23:05.7	50.8	8.1	0.2	2.51	35.0	6.6	5.4	1
104	I17455–2800	17:48:41.63	–28:01:44.6	–15.6	10	1.7	2.18	31.0	5.9	4.1	1
105	I17545–2357	17:57:34.49	–23:58:04.3	7.9	2.93	5.4	0.87	23.7	4.1	3.1	2
106	I17589–2312	18:01:57.87	–23:12:32.9	21.3	2.97	5.4	0.65	22.4	4.0	3.0	2
107	I17599–2148	18:03:01.83	–21:48:09.0	18.6	2.99	5.4	1.15	32.0	5.2	3.4	1, 2
108	I18032–2032	18:06:14.99	–20:31:35.4	4.3	5.15	3.4	1.27	32.1	5.4	3.5	2
109	I18056–1952	18:08:38.18	–19:51:49.0	66.7	8.55	1.6	2.32	25.1	5.7	4.4	2
110	I18075–2040	18:10:34.82	–20:39:16.1	31.5	3.08	5.3	0.27	23.0	3.0	2.2	2
111	I18079–1756	18:10:50.60	–17:55:47.2	18	1.83	6.6	0.44	25.6	3.9	2.6	2
112	I18089–1732	18:11:51.28	–17:31:33.4	33.5	2.5	5.9	0.90	23.4	4.3	3.1	2
113	I18110–1854	18:14:00.83	–18:53:28.2	37	3.37	5.1	0.87	28.9	4.8	3.2	2
114	I18116–1646	18:14:35.76	–16:45:40.8	48.5	3.94	4.6	0.99	33.8	5.1	3.1	2
115	I18117–1753	18:14:39.14	–17:52:01.3	36.7	2.57	5.9	1.02	23.6	4.6	3.5	2
116	I18134–1942	18:16:22.12	–19:41:27.0	10.6	1.25	7.1	0.23	20.7	3.0	2.4	2
117	I18139–1842	18:16:51.72	–18:41:35.2	39.8	3.02	5.4	0.45	40.4	4.9	2.5	2
118	I18159–1648	18:18:54.34	–16:47:51.9	22	1.48	6.9	0.48	21.6	3.8	2.8	2
119	I18182–1433	18:21:09.22	–14:31:46.8	59.1	4.71	4.1	0.71	24.7	4.3	3.1	2
120	I18223–1243	18:25:10.58	–12:42:24.2	44.8	3.37	5.3	0.83	23.7	4.2	2.9	2
121	I18228–1312	18:25:41.81	–13:10:23.3	32.3	3.21	5.4	0.81	29.8	4.7	3.0	2
122	I18236–1205	18:26:25.65	–12:04:01.6	25.9	2.17	6.3	0.62	19.5	3.5	2.9	2
123	I18264–1152	18:29:14.28	–11:50:27.0	43.2	3.33	5.3	0.81	20.3	3.9	3.2	2
124	I18290–0924	18:31:43.23	–09:22:28.5	84.2	5.34	4.0	1.09	22.1	4.0	3.2	2

Downloaded from https://academic.oup.com/mnras/article/496/3/2790/5854208 by Universidad de Chile user on 25 November 2020

Table A1 – *continued*

ID	IRAS	RA	DEC	V_{lsr} (km s^{-1})	Distance (kpc)	R_{GC} (kpc)	Radius (pc)	T_{dust} (K)	$\log(L_{\text{bol}})$ (L_{\odot})	$\log(M_{\text{clump}})$ (M_{\odot})	References ^d
125	I18308-0503	18:33:29.42	-05:00:55.1	42.9	3.1	5.7	0.59	31.0	4.3	2.6	1
126	I18311-0809	18:33:53.43	-08:07:14.4	113	6.06	3.7	2.12	25.4	5.0	3.7	2
127	I18314-0720	18:34:10.25	-07:18:00.1	101.5	5.82	3.9	2.54	30.4	5.7	3.8	2
128	I18316-0602	18:34:20.58	-05:59:41.6	42.8	2.09	6.5	0.56	23.4	4.0	2.9	2
129	I18317-0513	18:34:25.50	-05:10:53.5	42.1	2.18	6.5	0.32	31.0	4.8	3.2	1, 2
130	I18317-0757	18:34:24.90	-07:54:50.6	80.7	4.79	4.4	1.93	30.4	5.2	3.4	2
131	I18341-0727	18:36:49.82	-07:24:53.0	112.7	6.04	3.8	2.02	25.7	5.1	3.7	2
132	I18411-0338	18:43:46.07	-03:35:33.0	102.8	7.41	4.0	1.98	27.6	5.1	3.7	2
133	I18434-0242	18:46:03.51	-02:39:26.7	97.2	5.16	4.7	1.48	35.5	5.7	3.6	2
134	I18440-0148	18:46:36.22	-01:45:23.7	97.5	5.16	4.7	0.43	33.0	4.1	2.3	2
135	I18445-0222	18:47:09.76	-02:18:47.6	86.9	5.16	4.7	1.30	27.0	4.6	3.4	2
136	I18461-0113	18:48:41.83	-01:10:01.4	96.1	5.16	4.7	0.65	27.0	4.4	3.1	2
137	I18469-0132	18:49:33.15	-01:29:04.2	87	5.16	4.7	0.68	32.2	4.8	3.0	2
138	I18479-0005	18:50:30.79	-00:01:58.2	14.6	12.96	7.5	2.45	34.2	6.1	4.2	2
139	I18502+0051	18:55:22.63	00:59:16.0	53	7.1	4.7	1.24	30.0	5.3	3.9	1
140	I18507+0110	18:53:18.42	01:15:00.1	57.2	1.56	7.1	0.44	29.2	4.8	3.2	2
141	I18507+0121	18:53:18.12	01:25:22.7	57.9	1.56	7.1	0.29	22.7	3.5	2.6	2
142	I18517+0437	18:54:14.13	04:41:46.2	43.9	2.36	6.6	0.23	32.0	4.6	2.9	1, 2
143	I18530+0215	18:55:33.61	02:19:09.0	74.1	4.67	5.3	1.06	26.1	4.7	3.3	2
144	I19078+0901	19:10:13.41	09:06:10.4	2.9	11.11	7.6	4.26	33.3	6.9	5.0	2
145	I19095+0930	19:11:53.90	09:35:45.9	43.7	6.02	5.8	0.64	34.9	5.1	3.1	2
146	I19097+0847	19:12:09.09	08:52:10.8	58	8.47	6.2	2.01	23.3	5.0	3.8	2

^aReferences. 1: Faúndez et al. (2004); 2: Urquhart et al. (2018)

¹Shanghai Astronomical Observatory, Chinese Academy of Sciences, 80 Nandan Road, Shanghai 200030, People's Republic of China

²Korea Astronomy and Space Science Institute, 776 Daedeokdaero, Yuseong-gu, Daejeon 34055, Republic of Korea

³Department of Astronomy, The University of Texas at Austin, 2515 Speedway, Stop C1400, Austin, TX 78712-1205, USA

⁴University of Science and Technology, Korea (UST), 217 Gajeong-ro, Yuseong-gu, Daejeon 34113, Republic of Korea

⁵Jet Propulsion Laboratory, California Institute of Technology, 4800 Oak Grove Drive, Pasadena, CA 91109, USA

⁶Institute of Astronomy and Astrophysics, Academia Sinica, 11F of Astronomy-Mathematics Building, AS/NTU No. 1, Section 4, Roosevelt Road., Taipei 10617, Taiwan

⁷Center for Astrophysics, Harvard & Smithsonian, 60 Garden Street, Cambridge, MA 02138, USA

⁸National Astronomical Observatory of Japan, National Institutes of Natural Sciences, 2-21-1 Osawa, Mitaka, Tokyo 181-8588, Japan

⁹Kavli Institute for Astronomy and Astrophysics, Peking University, 5 Yiheyuan Road, Haidian District, Beijing 100871, People's Republic of China

¹⁰Department of Physics, University of Helsinki, PO Box 64, FI-00014 Helsinki, Finland

¹¹Departamento de Astronomía, Universidad de Chile, Las Condes, 7591245 Santiago, Chile

¹²School of Physics, University of New South Wales, Sydney, NSW 2052, Australia

¹³School of Space Research, Kyung Hee University, Yongin-Si, Gyeonggi-Do 17104, Republic of Korea

¹⁴National Astronomical Observatories, Chinese Academy of Sciences, Beijing 100101, China

¹⁵University of Chinese Academy of Sciences, Beijing 100049, China

¹⁶NAOC–UKZN Computational Astrophysics Centre, University of KwaZulu-Natal, Durban 4000, South Africa

¹⁷Astronomy Department, University of California, Berkeley, CA 94720-3411, USA

¹⁸Department of Astronomy, and Key Laboratory of Astroparticle Physics of Yunnan Province, Yunnan University, Kunming 650091, People's Republic of China

¹⁹IRAP, Université de Toulouse, CNRS, UPS, CNES, 31400, Toulouse, France

²⁰Indian Institute of Space Science and Technology, Thiruvananthapuram 695 547, India

²¹Department of Astronomy, Eötvös Loránd University, Pázmány Péter sétány 1/A, H-1117 Budapest, Hungary

²²Department of Astronomy, Peking University, 100871 Beijing, People's Republic of China

²³Departamento de Astronomía, Universidad de Concepción, Av. Esteban Iturra s/n, Casilla 160-C, Concepción, Chile

²⁴College of Science, Yunnan Agricultural University, Kunming 650201, People's Republic of China

²⁵Key Laboratory for Research in Galaxies and Cosmology, Shanghai Astronomical Observatory, Chinese Academy of Sciences, 80 Nandan Road, Shanghai 200030 People's Republic of China

²⁶Key Laboratory of Radio Astronomy, Chinese Academy of Sciences, Nanjing 210008, People's Republic of China

²⁷School of Physics and Astronomy, Sun Yat-sen University, 2 Daxue Road, Zhuhai, Guangdong 519082, People's Republic of China

²⁸SOFIA Science Centre, USRA, NASA Ames Research Centre, MS-12, N232, Moffett Field, CA 94035, USA

This paper has been typeset from a $\text{\TeX}/\text{\LaTeX}$ file prepared by the author.